CHALMERS
UNIVERSITY OF TECHNOLOGY

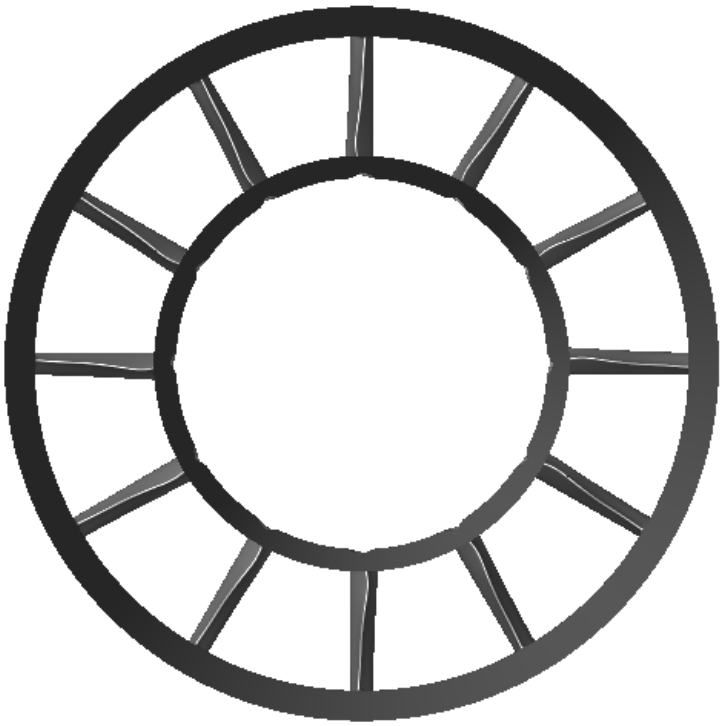

Aero-validation of CFD Methods for Turbine rear structures using experimental data

Master's thesis in Applied Mechanics

MATTIAS NILSSON

Department of Mechanics and Maritime Sciences
CHALMERS UNIVERSITY OF TECHNOLOGY
Gothenburg, Sweden 2019

Master's thesis 2019:16

Aero-validation of CFD Methods for Turbine rear structures using experimental data

MATTIAS NILSSON

CHALMERS
UNIVERSITY OF TECHNOLOGY

Department of Mechanics and Maritime Sciences
Division of Fluid Dynamics
CHALMERS UNIVERSITY OF TECHNOLOGY
Göteborg, Sweden 2019

Aero-validation of CFD Methods for Turbine rear structures using experimental data

MATTIAS NILSSON

Supervisor
Dr. Srikanth Deshpande
Hot Structures Department
GKN Aerospace Engine Systems, Sweden

Examiner
Prof. Lars Davidsson, Department of Mechanics & Maritime sciences
Division of Fluid Dynamics
Chalmers University of Technology, Sweden

Master's Thesis 2019:16
Department of Mechanics & Maritime Sciences
Division of Fluid Dynamics
Chalmers University of Technology
SE-412 96 Göteborg
Sweden
Telephone: +46-(0)31-772 1000

Cover: Rear view of the full annular geometry of the TRS, see figure 3.2.

Typeset in LaTeX
Göteborg, Sweden 2019

Aero-validation of CFD Methods for Turbine rear structures using experimental data

MATTIAS NILSSON

Department of Mechanics & Maritime sciences
Division of Fluid Dynamics
Chalmers University of Technology

Abstract

Secondary flow effects in an axial turbine are highly complex and have a significant impact on the performance of an aircraft engine. Understanding the flow in the engine is essential to improve the design and increase engine efficiency. In order to increase understanding of the aerodynamics in a Turbine Rear Structure (TRS) tests are conducted at experimental facilities. The resulting test data provides valuable input in improving the prediction tools used in the design of the TRS.

The aim of this study is to use computational fluid dynamics (CFD) simulations to increase the understanding of differences between prediction method results and experimental data.

The CFD predictions are compared to test data from a turbine test facility capable of reproducing realistic engine conditions. The same operating conditions as in the test facility are used on the same geometry to produce the numerical results. Comparisons of blade loading, swirl angle and total pressure profiles are made for design and off-design conditions using different turbulence models. For some cases, a heat transfer investigation is also conducted.

The results show how steady state simulations can be used to reproduce a close approximation of the experimental measurements for both design and off-design conditions.

Acknowledgements

I would like to acknowledge some contributions to this thesis and express my gratitude to those, who in different ways, have supported me throughout this project.

First and foremost, a great thank you to my supervisor at GKN Aerospace Engine Systems, Srikanth Deshpande, without whom this thesis would not be in the hand of the reader. Srikanth has been extremely supportive and gone above and beyond by making himself available to discuss and give inputs to the project while enabling me to learn and grow as an engineer.

Another thanks to Markus Nordahl, manager of the department of Hot Structures at GKN, for together with my supervisor considering me for the position. Markus has shown great support and understanding for the need of balance between work and private life, helping me remain grounded when under pressure during stressful times.

Several people have made significant contributions towards making this thesis what it is today. A special thanks to Hans Abrahamsson, Jonas Larsson, Pär Nylander and Linda Ström at GKN for sharing their knowledge, giving advice, showing interest for and supporting the project. I am very grateful for their guidance.

Thanks also to professor Lars Davidsson, head of the fluid dynamics division at Chalmers University of Technology, for taking his time to be the examiner of the project and assisting in administration.

Other colleagues have contributed by giving inputs, partaking in discussions and asking questions. The thesis improved thanks to their engagement.

Last but not least, thanks to Anna and my family for being patient and unconditionally supportive throughout the busiest period of my life so far.

Mattias Nilsson, Göteborg, June 2019

This project was made possible by GKN Aerospace Engine Systems in Trollhättan and Chalmers University of Technology in Gothenburg.

Nomenclature

Acronyms

ADP	Aerodynamic Design Point
CAD	Computer-aided design
CFD	Computational Fluid Dynamics
DS	Downstream
Exp	Experimental
HTC	Heat Transfer Coefficient
LPT	Low Pressure Turbine
MRF	Multiple Reference Frame
OGV	Outlet Guide Vane
OP	Operating pressure
PS	Pressure side
RANS	Reynolds Time-Averaged Navier-Stokes
rpm	Revolutions per minute
SS	Suction side
SST	Shear stress transport
TRS	Turbine Rear Structure
US	Upstream

Greek Symbols

α	Absolute flow angle [deg]
β	Relative flow angle [deg]
ω	Specific dissipation rate [1/s]
θ	Circumferential coordinate and sector pitch [deg]
ε	Turbulent dissipation rate $[m^2/s^3]$
φ	Under-relaxation factor [-]

Latin

$\dot{m}$	Massflow [kg/s]
C	Absolute velocity [m/s]
Cp	Pressure coefficient [-]
Cp_0	Total pressure coefficient [-]
k	Turbulent kinetic energy $[m^2/s^2]$
P_0	Total pressure [Pa]
P_s	Static pressure [Pa]
q_w	Wall heat flux $[W/m^2]$
T	Temperature [K]
V	Relative velocity [m/s]
y^+	Dimensionless wall distance [-]
Re	Reynolds number

Subscripts

0	Total quantity (eg. total pressure, total temperature)
ref	Quantitiy taken at reference point
s	Static quantity (eg. static pressure, static temperature)

Contents

List of Figures

List of Tables

1
Introduction

1.1 Background

At GKN Aerospace Engine Systems in Trollhättan diverse parts for commercial jet engines are designed and manufactured. One such component is the Turbine Rear Structure (TRS). In order to understand the complex aerodynamics of the TRS tests are conducted at different experimental facilities. The resulting test data provides valuable input for improving the the tools used to design new component.

Recently there have been a couple of test campaigns where the available data can be used to assess various CFD methods. It is of great importance to understand the differences in the prediction methods when compared to test results.

1.2 Aim

This project aims to investigate aerodynamic analysis methods in computational fluid dynamics (CFD) prediction tools by using the test data available from experimental facilities. The project also aims to increase understanding of the CFD predictions tools currently in use for design of the TRS.

1.3 Objectives

The objectives of the study is to

- Investigate if aerodynamic steady state analysis of a TRS can be used to approximate time-averaged experimental data
- Determine how the steady state cases should be setup and run
- Discuss the results and draw conclusions
- Recommend future work

2
Theory

This chapter outlines the theoretical background related to the investigation and discussion in the project.

2.1 Computational Fluid Dynamics

Computational Fluid Dynamics is a field of fluid dynamics where numerical methods are used for modeling the differential equations governing conservation of mass, momentum and energy (Navier-Stokes equations) in a viscous fluid. Solving the equations numerically give good estimates of almost any geometry which can be used to analyze the flow of a gas or liquid. The most common form of the Naver-Stokes equations solved are the Reynolds Time-Averaged Navier-Stokes (RANS) equations.[1]

CFD has developed rapidly during the past decades, mainly due to the huge increase in computational power and improvement in numerical methods. Nowadays CFD is used extensively within most fields for engineering design, research and development. [1], [2]

In CFD, the geometry is spatially discretized into a finite number of elements called cells. This spatially divided numerical grid is referred to as a surface or volume mesh. In each mesh cell the RANS equations are solved for the flow quantities (e.g pressure, velocity and temperature) and their fluxes are computed over the cell boundaries to get the complete flow field in the entire domain. Starting from an initial solution and known boundary conditions the flow field is calculated iteratively until a converged solution is acquired. [1], [3]

2.1.1 Turbulence modeling

When time averaging the Navier-Stokes equations the resulting RANS equations contain unknown turbulent stress terms. These have to be modeled using a turbulence model. There are many turbulence models available, e.g realizable $k\varepsilon$ ($rk\varepsilon$), $k\omega$-SST and transition-SST. Each turbulence model, formulated for different flow conditions, is practical in different situations. The inherent difference in the turbulence models will lead to different numerical results. [3], [4]

2.1.2 ANSYS Fluent

ANSYS Fluent is a commercial CFD solver used to model fluid flow, turbulence, heat transfer, and reactions for industrial applications. Some examples of applications that can be simulated in Fluent are air flow over an aircraft wing, oil ocean platforms, combustion in a furnace, semiconductor manufacturing, blood flow in the human body and wastewater treatment plants. Fluent also includes capabilities to model aero-acoustics, turbomachinery and multiphase flow. [5]

2.1.3 Under-relaxation

Under-relaxation factors are used in ANSYS Fluent as a way of controlling the rate of change of the flow quantities allowed to take place between iterations. Each iteration, a flow quantity φ changes according to equation 2.1

$$\varphi = \varphi_{old} + \alpha\Delta\varphi, \quad \alpha \leq 1 \tag{2.1}$$

where α is the under-relaxation factor.

If $\alpha < 1$ the flow quantity φ will change less than the calculated change $\Delta\varphi$ resulting in slower changes. If changes in the flow field are too large between iterations the solution can become unstable and diverge. Under-relaxation can increase stability and help control convergence by limiting how fast the flow field is allowed to change between iterations. [6]

The trade-off when using low under-relaxation factors for stability is that computational time increase as more iterations are generally needed to reach the converged solution. For this reason the solution can be initiated running on low under-relaxation factors and subsequently raising them as the final solution is approached.

2.1.4 Mesh interfaces

If a computational domain is made up of more than one mesh, the solver has to be told how to deal with the interface where the two (or more) meshes intersect. This intersection is called a mesh interface. An example of mesh interfaces between three regions of separately created meshes is shown in figure 2.1

The mesh interface can, for example, be a solid wall where no fluid is allowed to pass through it, or an interior surface where the two meshes are treated as if they were one, allowing fluid to pass freely. Several ways of treating the mesh interface will be investigated in this study, including the "normal" mesh interface, the mixing

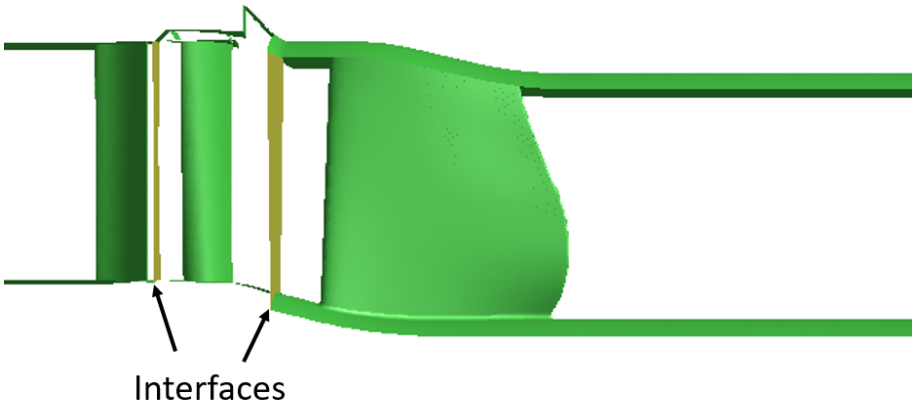

Figure 2.1: Mesh interfaces

plane model and the turbo interface presented in the following sections.

2.1.4.1 Normal mesh interface

When the mesh surfaces joining at the interface are the same size and have the same number of elements aligned to match 1:1 the meshes are called conformal meshes. For conformal meshes, it is possible to use a normal mesh interface. For the normal mesh interface the solver calculates the flux across the cell faces as if the meshes were one.

If a normal interface is used with non-conformal meshes, where the mesh does not align, new faces are produced only where cells from the two sides of the interface overlap. The fluxes are then calculated across the new faces.

The mesh interface allows the two surfaces to be offset from each other as long as some part of the surfaces intersect. By default, offset mesh interfaces are created with interior faces (allowing fluid to pass) where the meshes intersect and with wall faces where the meshes do not intersect. This can be changed to for example produce only interior cells or only wall cells. Regardless, the normal mesh interface requires the mesh interface to be the same size for both meshes. [6]

2.1.4.2 Mixing Plane Model

To discretize the whole geometry in an axial turbine with sufficient resolution results in large meshes requiring a lot of computational power. To save computational time, because the axial turbine is axisymmetric, the domain can be split up into single blade sectors at each blade row with a circumferential periodicity boundary condition on the domain sides.

In a multistage axial turbine the number of blades is usually different for each blade row. Therefore, each blade row domain will have a different circumferential angle

and the resulting meshes are no longer matching 1:1. As a result, the normal mesh interface discussed above cannot be used in such situation.

For situations where maintaining circumferential periodicity is not feasible, for example when the resulting mesh becomes too large, the mixing plane model can be a cost-effective alternative.

In the mixing plane model, each fluid domain is treated as a steady-state problem. Flow-field data from adjacent zones are passed as boundary conditions that are spatially averaged or “mixed” at the mixing plane mesh interface. This mixing removes any unsteadiness that would arise due to circumferential variations in the passage-to-passage flow field, for example, wakes, shock waves and separated flow. Therefore the results is a "mixed out" steady-state approximation.[6]

Despite the simplifications inherent in the mixing plane model, the resulting solutions can provide reasonable approximations of the time-averaged flow field.

When creating a mixing plane mesh interface a radial interface profile is created from circumferential averaging of the flow quantities at discrete radial points which is then passed as boundary conditions to the adjacent zone. Depending on the boundary condition of the mixing plane different flow quantities are preserved across the interface. The following boundary conditions are available to use for the mixing plane interface. [6]

- Velocity inlet (incompressible flow only)
- Mass flow inlet
- Pressure inlet

For the velocity inlet, the upstream velocity is preserved and passed as a boundary condition on the downstream side of the interface. Similarly, the mass flow inlet and pressure inlet pass the mass flow and static pressure respectively, conserving these quantities across the interface.

While using the mixing plane model care must be taken to avoid backflow over the interface as the mixing plane is very sensitive to reverse flow.

2.1.4.3 Turbo interface

In the BETA features of Fluent v2019R1 there is another choice of mesh interface called turbo interface. The turbo interface is specifically being added for the purpose of running simulations on non-conformal meshes in turbomachines and has more options for taking difference in circumferential sector size into account. Some of these setting tries to compensate for difference in pitch by stretching the smaller interface onto the larger. There are three different choices for the pitch-change type of the turbo interface; pitch-scale, no pitch-scale and mixing plane.[6]

The pitch-scale interface takes the interface flow profile between the cell zones and stretches or compresses it to match, in order to maintain the interaction between blade row passages. To retain acceptable solution accuracy it is recommended not to use the pitch-scale interface if the difference between pitch ratio between the two domains is more than 20%. As currently implemented in the BETA features the interface cannot be created if this pitch-ratio limit is surpassed. [6]

The no pitch-scale interface maintains the blade row interaction by creating virtual copies of the smaller interface onto the larger interface. This option is available for any difference in pitch.

Finally, the turbo interface mixing plane is similar to the mixing plane model that is already available in Fluent except from the use of the pitch-scale model. Regardless of if there are any differences in pitch angle or not between the interfaces the pitch-scale model is used to scale one interface onto the other. Therefore the two models share limitations, for example not giving reliable results if the pitch-angle difference is larger than 20%. A difference, however, is that the turbo interface mixing plane can be used even if this limit is exceeded.

The turbo interface mixing plane only provides 10 interpolation points in the radial direction and cannot be changed unlike for the normal mixing plane. Therefore this mixing plane gives very rough profiles compared to the normal mixing plane where the number of radial interpolation points can be increased up to the number of mesh cells in the radial direction. The turbo interface mixing plane is currently limited to pitch-changes up to a ratio of 3:1 but will be available for any pitch-change in the future. [6]

2.2 Turbomachinery

Turbomachines are defined as devices that transfer energy either to or from a continuously flowing fluid by the dynamic action of one or more moving blade rows. The two main categories of turbomachinery are those that consume power to increase fluid pressure or those that produce power by expanding a fluid, lowering its pressure. The first category contains machines such as fans, compressors and pumps while wind, hydraulic, steam and gas turbines are in the second category.

Turbomachines can be further divided into categories based on how the flow passes through the rotor. An axial flow turbomachine has the through-flow mainly parallel to the axis of rotation whereas a radial flow turbomachine mainly has the flow perpendicular to the axis of rotation. [7], [8]

2.2.1 Turbine Rear Structures

The TRS is a an aircraft engine component mounted at the rear end of the engine. The purpose of the TRS is to provide structural support, an interface for mounting to the rest of the aircraft and to increase aerodynamic performance by straightening the exit flow (see section 2.2.2). An example an TRS in the GP7200 engine is shown in the red box in figure 2.2

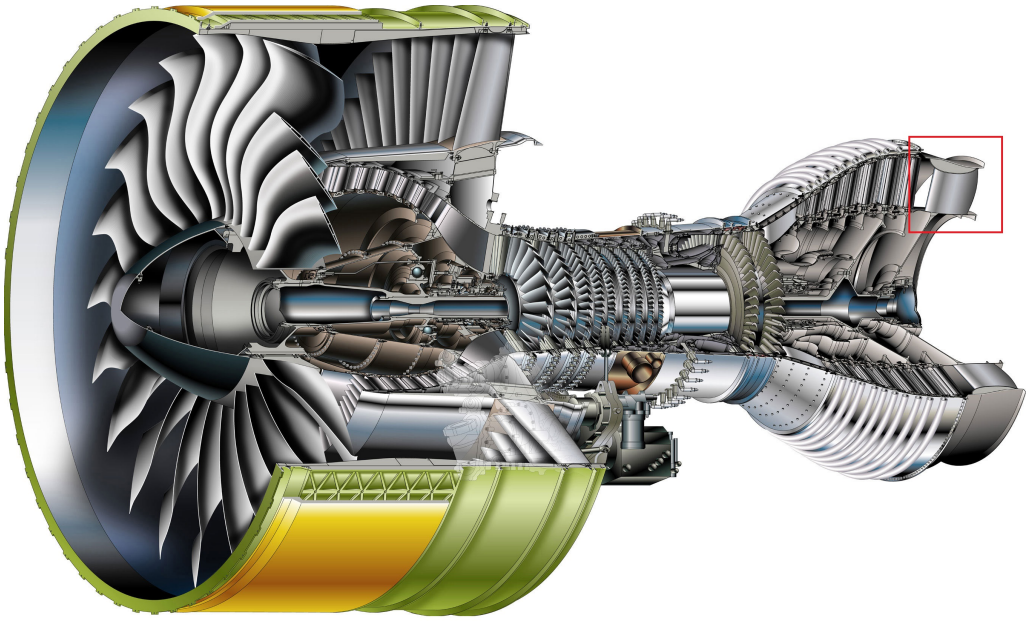

Figure 2.2: Cutaway of the GP7200 [9] - TRS in red box

2.2.2 Outlet Guide Vanes

When ejecting the flow in a jet behind the engine, it is desirable for the flow to be as axial as possible to get maximum net momentum thrust in the intended direction. By increasing the by-pass ratio of an aircraft engine the energy efficiency can be increased. However, this change in design has increased inlet swirl angles into the TRS making the aerodynamic design more demanding.[10]

The TRS aerodynamic purpose is to straighten the incident flow before it leaves the engine. This is done by stationary OGVs distributed circumferentially inside the TRS. An example of an OGV is shown in figure 2.3. The secondary flow effects related to the OGV are complex and highly affected by boundary conditions.

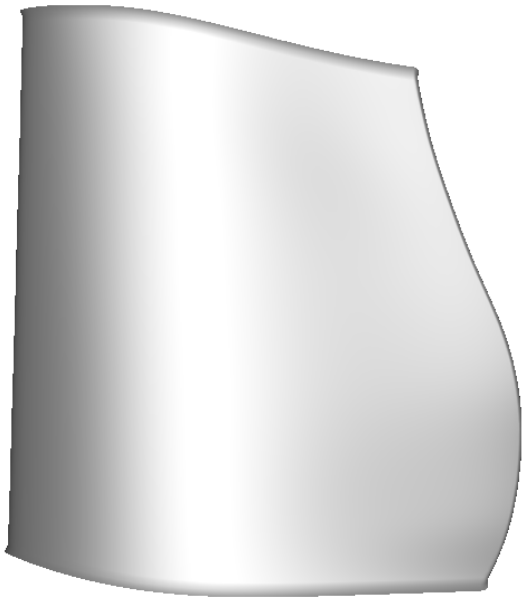

Figure 2.3: Side view of an OGV

2.2.3 Swirl angle

The velocity triangles of a turbine stage in an axial flow turbine are shown in figure 2.4. [8] Gas enters through the nozzle blades (also called stator blades or nozzle guide vanes) with velocity C_1 at an angle α_1 to the axial direction. The flow is then turned and leave the nozzle blades with an increased velocity C_2 at an angle α_2. Similarly, after being deflected and expanded through the moving rotor blades, the flow exits the stage with velocity C_3 at an angle α_3. The angle α_3 is known as the swirl angle. [8]

The swirl angle is used in this study for comparing numerical data to experimental data. It will therefore be referred to many times throughout the investigation, analysis and discussion.

When the flow leaves the turbine and enters the TRS it has an inlet swirl angle as described above. The OGV then turns the flow and reduces the outlet swirl angle as shown in figure 2.5.

From trigonometry the swirl angle can be defined as (see figure 2.4)

$$\alpha_3 = arctan\left(\frac{C_{w3}}{C_{\alpha 3}}\right) = arctan\left(\frac{V_\vartheta}{V_x}\right) \tag{2.2}$$

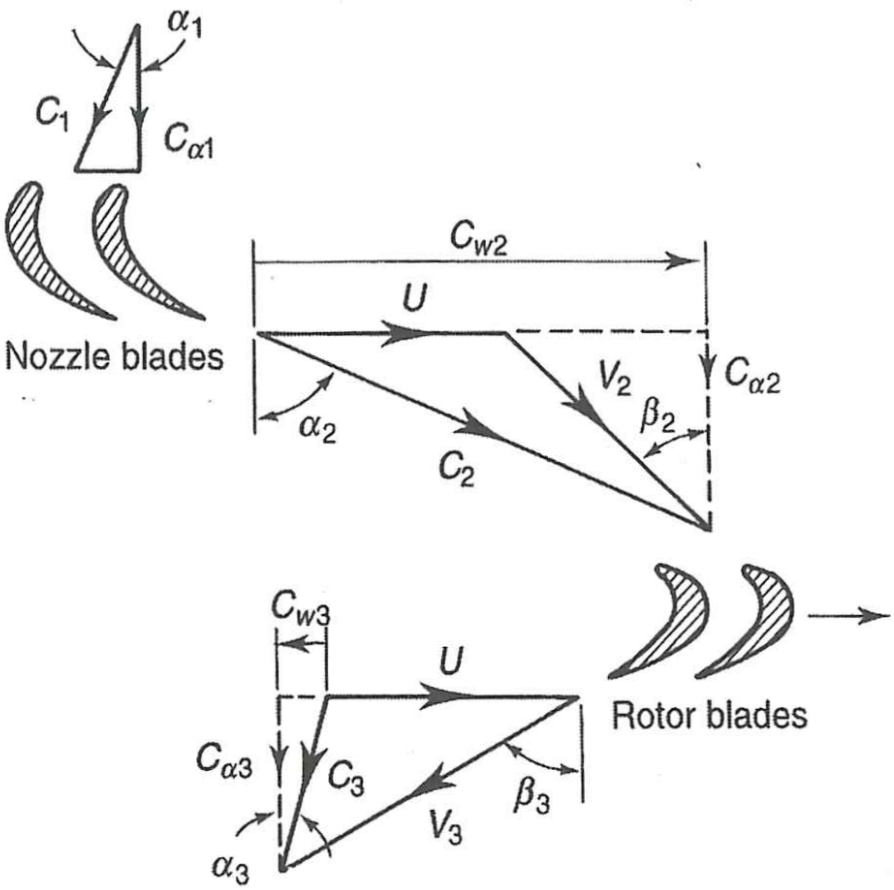

Figure 2.4: Velocity diagram of an axial flow turbine stage. [8]

Figure 2.5: OGV turning the incident flow effectively reducing the swirl

2.2.4 Blade loading

Knowing the pressure distribution around an aerofoil, the lift force can be calculated by integrating the pressure around the blade. This integral corresponds to the area enclosed by the pressure distribution plotted around the blade. If plotted at a certain span, the area enclosed by the pressure curves is then the lift force due to the pressure distribution on the blade at that span. [2]
An example of a pressure coefficient distribution along the surface of an OGV one span section is shown in figure 2.6.

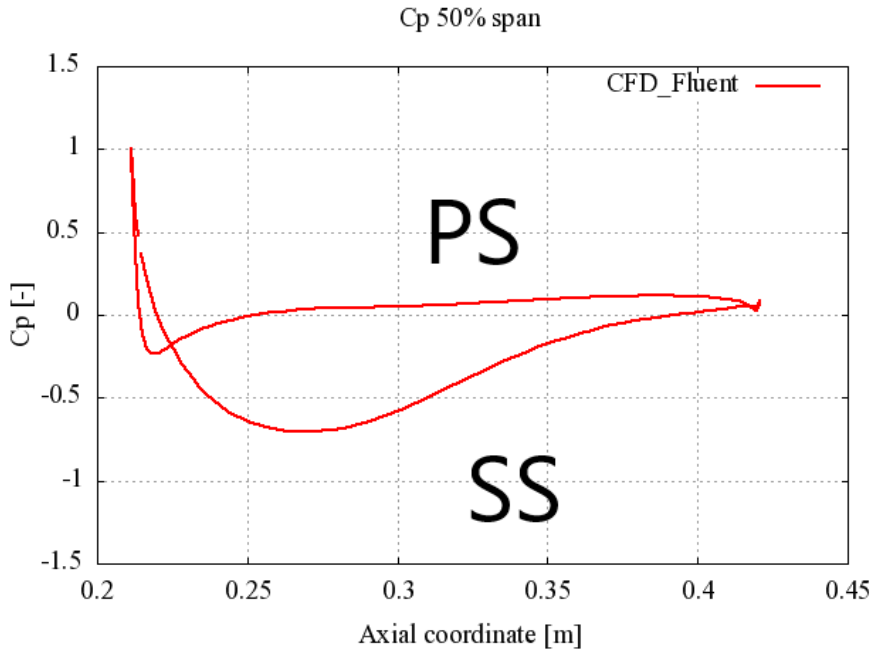

Figure 2.6: Pressure coefficient distribution along the surface of an OGV at one span section

A larger area means a higher lift force and therefore higher loading of the blade. Hence, the blade loading is directly related to the area enclosed by the pressure distribution around the blade as discussed above. Like the swirl angle, blade loading will be used when comparing numerical results to the test data in this study and will be referred to frequently. An example of an OGV blade is shown in figure 2.7, where the pressure side (PS) and suction side (SS) of the blade has been denoted. Figure 2.7b and 2.7c shows a side view the pressure side and suction side of the blade, respectively, where a span section line has also been marked.

2.3 Experimental setup

The test facility providing the experimental data used for investigation in this thesis is a closed loop wind tunnel driven by a centrifugal fan. The flow is led through

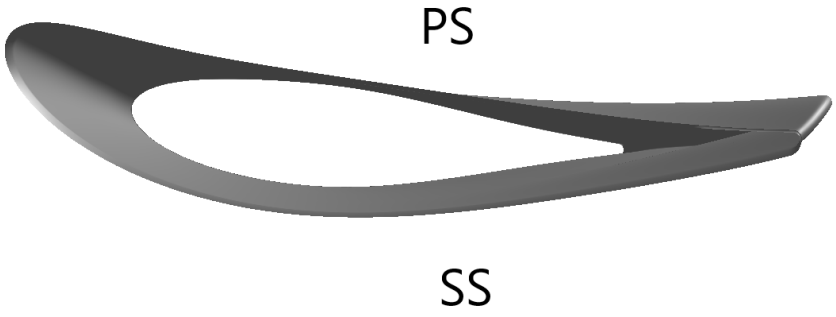

(a) Top view

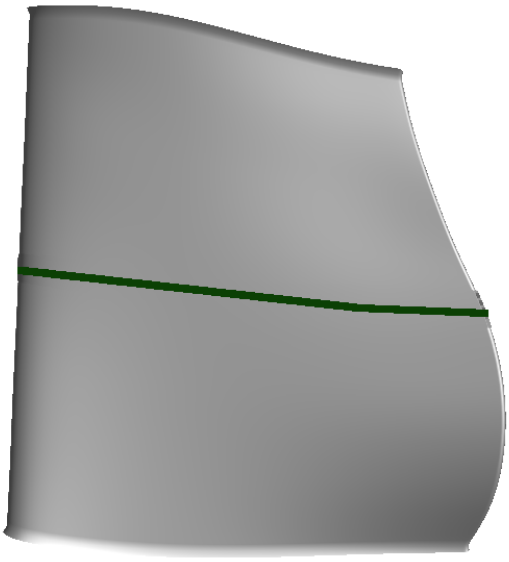

(b) Pressure side

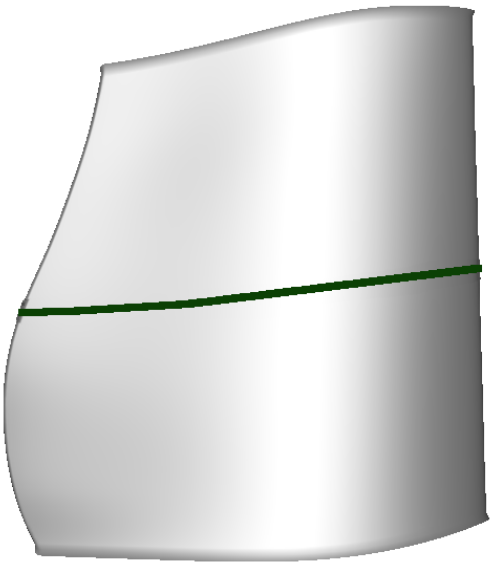

(c) Suction side

Figure 2.7: Example blade

diffusers into a heat exchanger and settling chamber used for flow conditioning. Finally the flow is accelerated through a contraction before entering into a low pressure turbine (LPT) section. The LPT is used to provide realistic engine conditions for the inlet boundary to the test TRS mounted at the end of the LPT. An illustration of the experimental facility is shown in figure 2.8. [10]

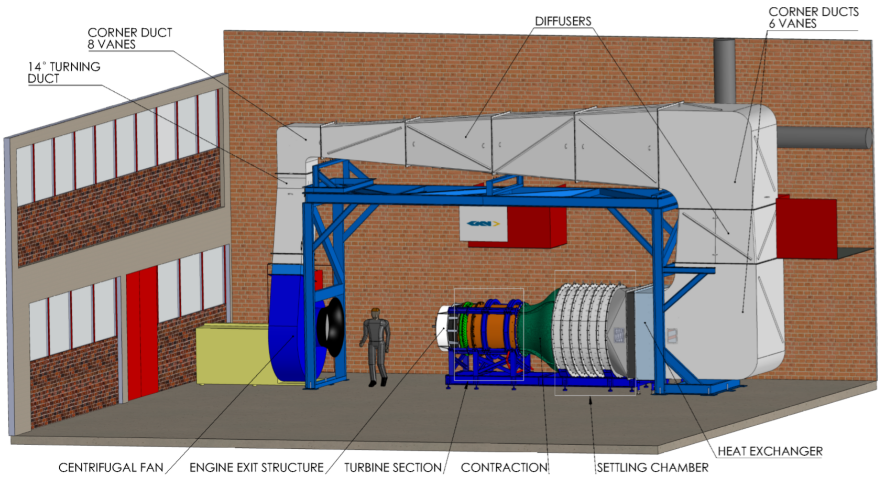

Figure 2.8: Illustration of the experimental facility [10]

Measurement data is taken at two measurement planes inside the TRS. One is located upstream (US) of the OGV and one downstream (DS) of the OGV as shown in figure 2.9. Since the flow is known to be highly three-dimensional with complex flow features such as secondary flow effects and wakes, multi-hole probes are used to characterize the flow at these planes. At the US measurement plane a five-hole probe is used and at the DS measurement plane a seven-hole probe is used. Both probes face the incoming flow parallel to the axial direction.

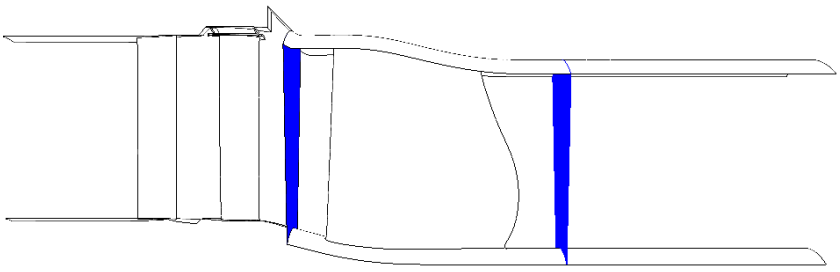

Figure 2.9: Measurement planes in the test rig

Blade loading data is acquired using a 3D printed OGV with pressure taps as shown in figure 2.10. In this study blade loading extracted at 25%, 50% and 75% span is used. [10]

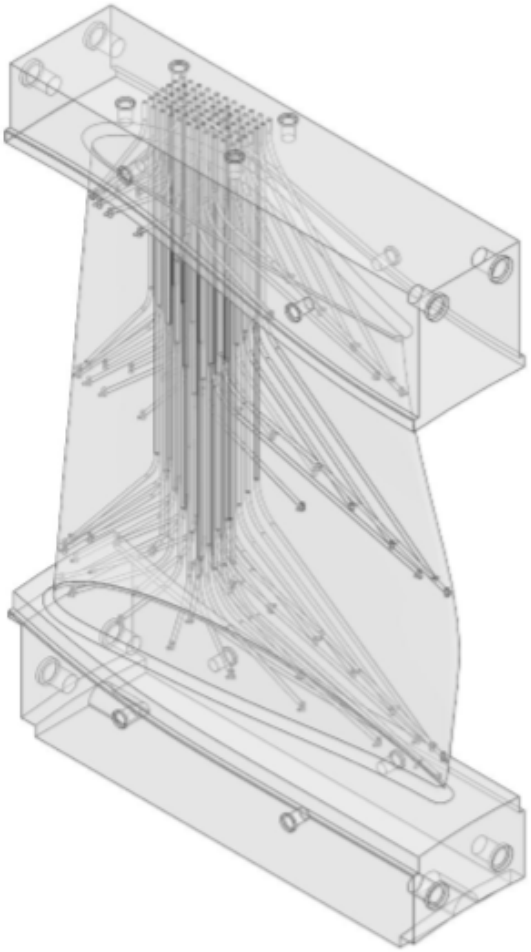

Figure 2.10: 3-D printed OGV with pressure taps [10]

For details on the experimental facility layout, instrumentation, commissioning and performance evaluation see [10].

2.3.1 Reference point and pressure coefficients

In the experimental facility a reference Prandtl tube is located between two of the OGVs near mid span and mid axial chord as shown in figure 2.11.

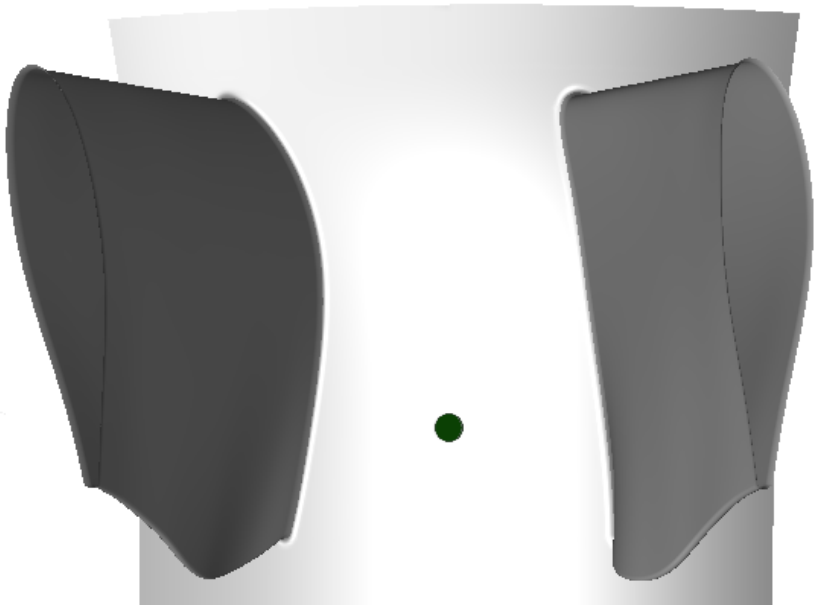

Figure 2.11: Reference point

At this point the reference pressure is used to define a pressure coefficient as [10]

$$Cp = \frac{P_s - P_{s,ref}}{P_{0,ref} - P_{s,ref}} \tag{2.3}$$

Similarly, a total pressure coefficient is defined as

$$Cp_0 = \frac{P_0 - P_{0,ref}}{P_{0,ref} - P_{s_ref}} \tag{2.4}$$

3
Methods

This chapter describes the methods used to generate the results in the project.

3.1 Geometry

The geometry that was analyzed consists of 60 stator blades, 72 rotor blades and 12 OGVs in the TRS. The full annular CAD-model is shown in figure 3.1.

(a) Front view (b) Iso view (c) Rear view

Figure 3.1: Full annular geometry of the three domains

The component of interest for investigation in this study was the TRS, shown in figure 3.2.

3.1.1 Computational domain

Running simulations on the full annular geometry with a high resolution would result in a huge mesh that would require a lot of computational time. Because the geometry is axisymmetric it was instead divided into three regions with one stator blade, one rotor blade and one OGV respectively. The computational domain with the three regions is shown in figure 3.3.

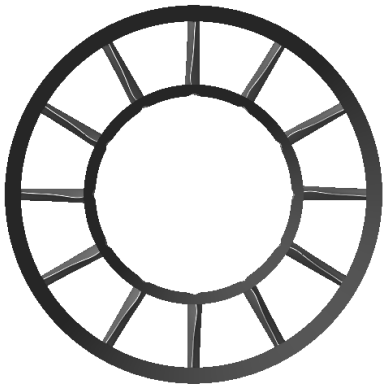

Figure 3.2: Rear view of the full annular geometry of the TRS

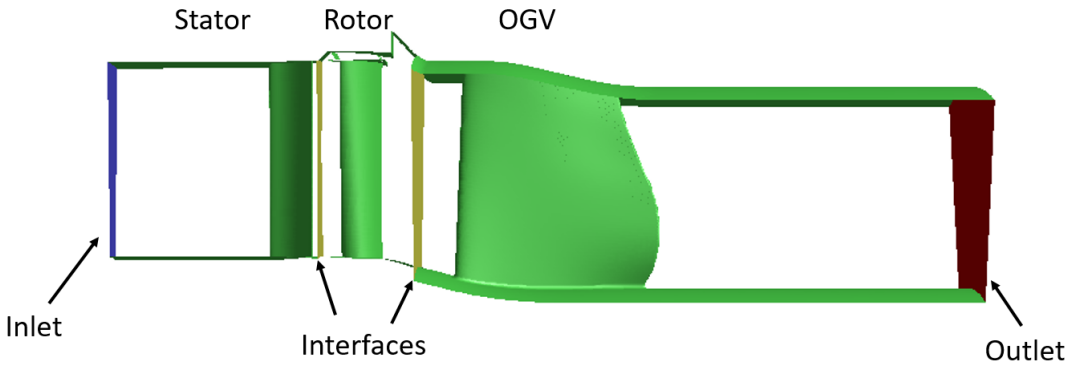

Figure 3.3: Computational domains and boundaries

The boundaries are the stator inlet, OGV outlet and rotational periodicity boundaries on the sides. The inlet boundary condition is a mass flow inlet and the outlet is a pressure outlet. The interfaces where the regions intersect are also marked in yellow in figure 3.3. All other surfaces, shown in green, are solid adiabatic walls.

The simulations were performed using the Multiple Reference Frame (MRF) model. The MRF model allows for different reference frames in different part of the computational domain. Here, the stator and OGV regions will have stationary reference frames while the rotor regions will have a moving reference frame.

The rotor reference frame was given a rotational speed and the moving parts in the rotor were set to moving walls with 0 rotational speed relative to the reference frame. This simulates the effect of the rotation in the rotor without having to run simulations with a moving mesh. [6]

Since the OGV is the component of interest one may ask why simulations were not carried out on the OGV region only, simplifying the problem by disregarding the stator and rotor regions. The reason the calculations were carried out on the stator, rotor and OGV domains using the MRF model was to replicate the inlet boundary conditions at the inlet of the OGV region using the CFD models only.

Say, for example, that the test facility is run with a mass flow $\dot{m} = 10kg/s$ and a rotational speed 600 rpm. The flowfield can then be measured and the measured profiles at the US measurement plane can be applied to the OGV inlet in the CFD model as a boundary condition.

What if there is a desire to predict the case of $\dot{m} = 11kg/s$ and 650 rpm? Then the boundary conditions at the inlet to the OGV are again unknown and measurements have to be conducted in the test facility before the prediction model can be used. This defeats the purpose of using the prediction model in the first place.

If instead the stator, rotor and OGV are used in the computational model the desired massflow can be set as an inlet boundary condition to the stator and the desired rotational speed can be set as the rotational speed of the reference frame in the rotor domain. The purpose of the stator and rotor domains are then to produce close approximations to the inlet boundary conditions when compared to the experimental data.

For this reason the measurements at the US plane is interesting for the purpose of validation of the prediction models. If this method results in accurate approximations of the experimental data any conditions can be predicted by the CFD methods by only knowing the massflow through the engine and the rotational speed of the axis.

3.1.2 Non-conformal meshes

As discussed in section 3.1.1, to save computational power it is desirable to only simulate flow over one stator blade, one rotor blade and one OGV instead of the full annular geometry. However, because the full geometry consists of 60 stator blades, 72 rotor blades and 12 OGV blades the three regions will end up with different angles in the θ-coordinate direction. For the stator domain,

$$\theta_{strdom} = \frac{360°}{60} = 6^{\circ} \tag{3.1}$$

Similarly,

$$\theta_{rtrdom} = 5°, \quad \theta_{OGVdom} = 30° \tag{3.2}$$

This is visualized by considering the whole computational domain shown from above in figure 3.4

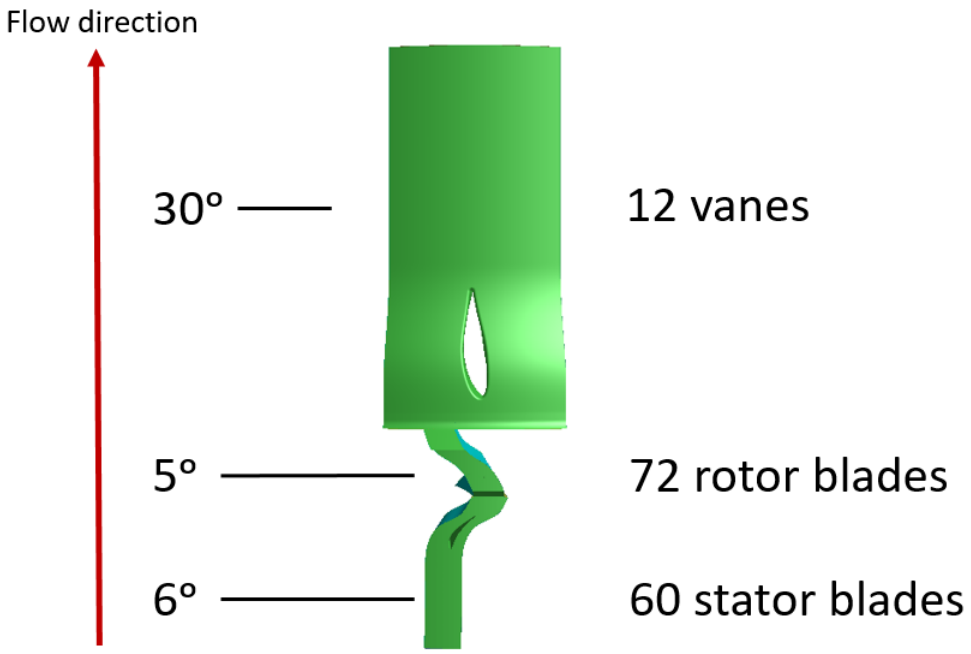

Figure 3.4: Top view of the computational domain

Dividing the regions into single blade sectors results in a computational domain with non-conformal meshes. This has to be taken into account when connecting the meshes in ANSYS Fluent and will be further discussed in section 3.3

3.1.2.1 Moving the stator blade

As outlined in section 2.1.4.2 the mixing plane model is very sensitive to reverse flow across the interface. Behind the stator the mesh interface is located very close to the stator trailing edge as seen in figure 3.5a.

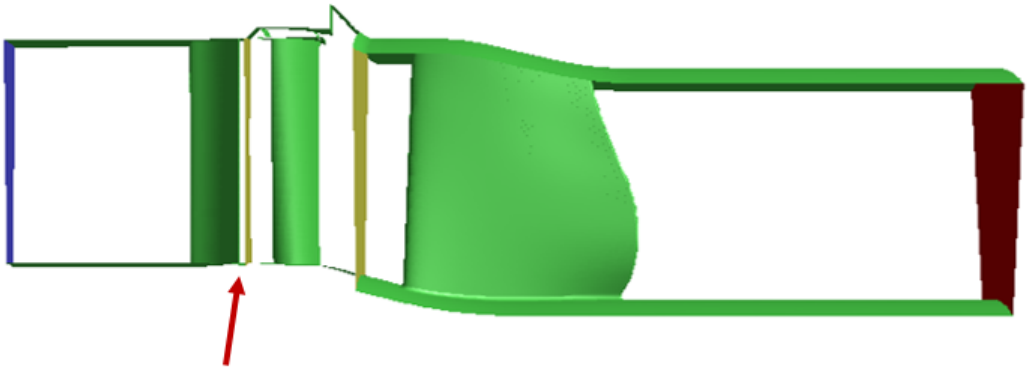

(a) Before

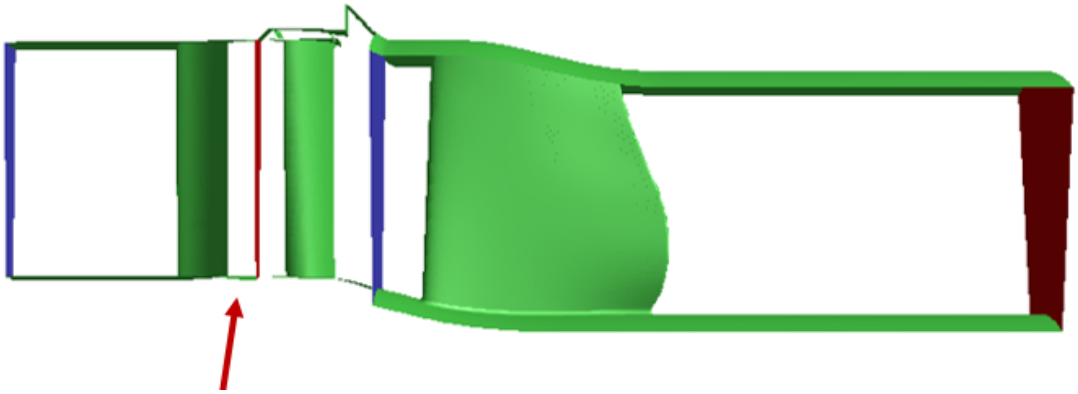

(b) After

Figure 3.5: Stator blade before and after being moved upstream

The separated flow near the trailing edge of the stator blade is observed to result in circulating flow and consequently reverse flow in many cells across the following mixing plane. Therefore the stator had to be moved slightly upstream as shown if figure 3.5b to achieve a converged solution. All simulations run using the mixing plane model at the mesh interfaces used the computational domain with the stator moved upstream.

The flow behind the stator is mixed out, removing any wakes and secondary effects, and then passed through the rotor and another mixing plane before reaching the OGV. Because the OGV is the part of interest in this study, a small change in flow behavior in the stator region that may result from moving the stator slightly upstream is out of the scope of this study.

3.1.3 Measurement planes

To be able to compare the experimental data and the numerical data from the simulations the numerical data must be extracted at the same locations in the numerical domain as in the experimental facility. The experimental data was taken at two measurement planes using pressure probes as described in section 2.3. The blade loading data was taken at 25%, 50% and 75% span. Figure 3.6 shows the measurement planes placed at the same locations in the numerical domain.

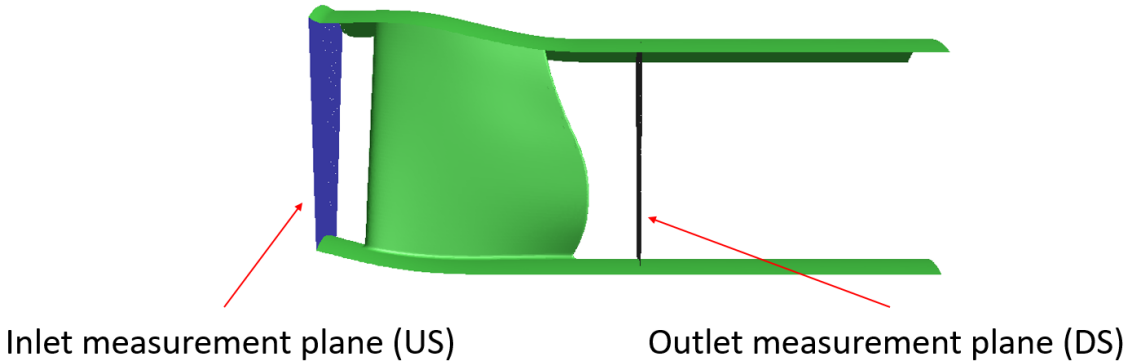

Figure 3.6: Measurement planes in the OGV domain

3.2 Mesh dependency study

To ensure that the numerical solution is independent on the spatial discretization a mesh dependency study was performed. Provided that the solution is not changing significantly with the finest mesh, three different meshes were to be investigated as shown in table 3.1. Only the OGV domain mesh was considered using the $rk\epsilon$ turbulence model. The mesh was also be checked to provide a wall y^+ close to 1 in most of the domain.

Mesh	No. cells	Mesh scale factor
Baseline	1735248	1
Intermediate	2547372	1.47 (1.5)
Fine	3519230	2.02 (2)

Table 3.1: Meshes considered for mesh dependency study

In addition to checking that y^+ is close to 1, the pressure loss was calculated over the OGV and compared for the three different meshes. With a satifactory y^+ and a pressure drop not changing significantly with mesh size, a mesh was to be chosen for the rest of the simulations.

3.3 Connecting the meshes

When importing the three different meshes into ANSYS Fluent three separate fluid domains are created. As discussed in section 2.1.4, for Fluent to understand that the domains are connected, mesh interfaces must be defined between the meshes.

3.3.1 Normal mesh interface

Tests to try connecting the normal meshes using the mesh interfaces were made despite the requirement that the meshes must match 1:1 will not be fulfilled. Non-overlapping faces in regular mesh interfaces become walls by default but were changed into interior cells. Since the requirements for the mesh interface is not fulfilled convergence was not expected.

3.3.2 Mixing plane

When simulating steady state conditions in rotating turbomachienery the mixing plane model is normally used. [6] The mixing plane model was tested and will be the primary interface of interest in this study.

3.3.3 Turbo interface

The pitch-scale, no pitch-scale and turbo interface mixing plane model were also tested. These are currently subjected to limitations as discussed in section 2.1.4.3 and are not expected to yield accurate results.

3.4 Investigating baseline settings

To investigate what baseline settings should be used to replicate the test data in Fluent simulations different setups were tested.

3.4.1 Difference in operating pressure

Most pressure definitions in Fluent are defined relative to the operational pressure as gague pressures. For instance, operational pressure 0 Pa and an outlet pressure of 101325 Pa gauge should yield the same results as operational pressure 101325 Pa and an outlet pressure of 0 Pa gauge.

There are however some numerical advantages setting the operational pressure as close to the pressure in the domain as possible. [1], [6] Both methods were investi-

gated to ensure no significant changes in the results are observed.

3.4.2 Mixing plane boundary conditions

For the mixing plane two of the three boundary condition options introduced in section 2.1.4.2 were tested; mass flow inlet and pressure inlet. Although the flow velocity in the test rig is low the simulations used a compressible flow solver and hence the velocity inlet could not be used. [6]

3.4.3 Difference in mixing plane under-relaxation

Under-relaxation was changed to adjust rate of change between iterations across the mixing plane. The investigation looked at difference in results between two different under-relaxation factors; the default value of 0,05 and double the default value 0,1.

3.5 Steady state CFD analysis

The steady state analysis investigated four operating conditions. One aerodynamic design point (ADP) and three off-design points; ADP0 , ADP+5, ADP+10 and ADP-10 respectively. The off-design points represent cases where the OGV inlet swirl has been offset from its design condition.

The four conditions were considered with two different Reynolds number cases; low Reynolds number and high Reynolds number. The cases corresponds to the Reynolds numbers used in the testing rig, 2.35E5 and 4.65E5 respectively. [10]

For each variation (aerodynamic design point + Reynolds number) three turbulence models were tested; $rk\varepsilon$, $k\omega - SST$ and an SST-transition model. The steady state cases that were simulated and compared to experimental data are summarized in table 3.2. These cases were chosen based on the experimental data available.

Primarily, comparison was made of inlet swirl angle, blade loading and total pressure coefficient.

3.6 Heat Transfer

Two different wall temperature cases were simulated and compared to available test data. All adiabatic walls in the OGV domain were changed to constant temperature walls and the wall temperature was set to

ADP	Reynolds number	Turbulence model
ADP0	Low	$rk\varepsilon$
ADP0	High	$rk\varepsilon$
ADP0	Low	$k\omega - SST$
ADP0	High	$k\omega - SST$
ADP0	Low	$SST - transition$
ADP0	High	$SST - transition$
ADP+5	Low	$rk\varepsilon$
ADP+5	Low	$k\omega - SST$
ADP+5	Low	$SST - transition$
ADP+10	Low	$rk\varepsilon$
ADP+10	High	$rk\varepsilon$
ADP+10	Low	$k\omega - SST$
ADP+10	High	$k\omega - SST$
ADP+10	Low	$SST - transition$
ADP+10	High	$SST - transition$
ADP-10	High	$rk\varepsilon$
ADP-10	High	$k\omega - SST$
ADP-10	High	$SST - transition$

Table 3.2: Cases considered for steady state study

$$\Delta T = T_{OGVinlet} \pm 20K \tag{3.3}$$

where $T_{OGVinlet}$ was based on the total temperature of the air at the inlet to the OGV domain, i.e the US measurement plane. If the variation in total temperature is small, the inlet air total temperature was to be assumed to be constant and chosen as a radial average of the inlet total temperature profile.

To visualize and compare heat transfer, the heat transfer coefficient (HTC) was defined as

$$HTC = \frac{q_w}{\Delta T}\left[\frac{W}{m^2K}\right] \tag{3.4}$$

Measured data of HTC was only available at 50% span. The HTC was however additionally presented as contour plots on the OGV blade.

To investigate impact of different turbulence models for heat transfer simulations of the OGV the same three models used in the steady state analysis were tested and compared.

4

Results and Discussion

This chapter presents the results of the investigation outlined above. The results are discussed and analyzed as they are presented.

4.1 Mesh dependency study

The total pressure loss over the OGV blade for the three different meshes outlined in table 3.1 is shown in figure 4.1. For the high Reynolds number case the change in total pressure drop between the three meshes is not significant. For the low Reynolds case the pressure drop increases by about 25% moving from the baseline mesh to the intermediate mesh.

Figure 4.2 shows the change in total pressure coefficient drop over the OGV blade. As expected from the total pressure drop difference between the baseline mesh and the intermediate mesh a similar change is observed for the low Reynolds case.

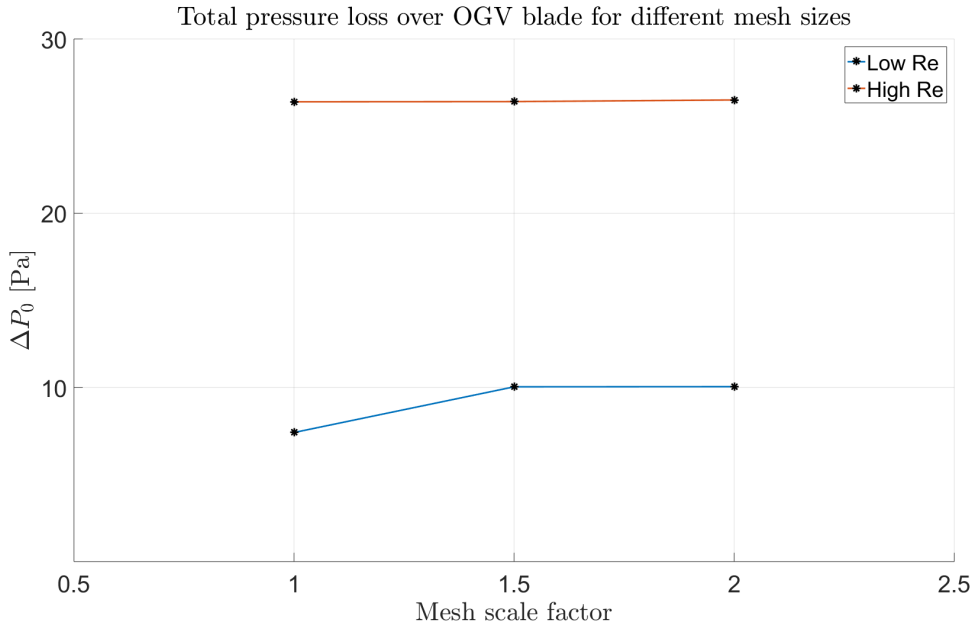

Figure 4.1: Total pressure loss over OGV blade for different meshes

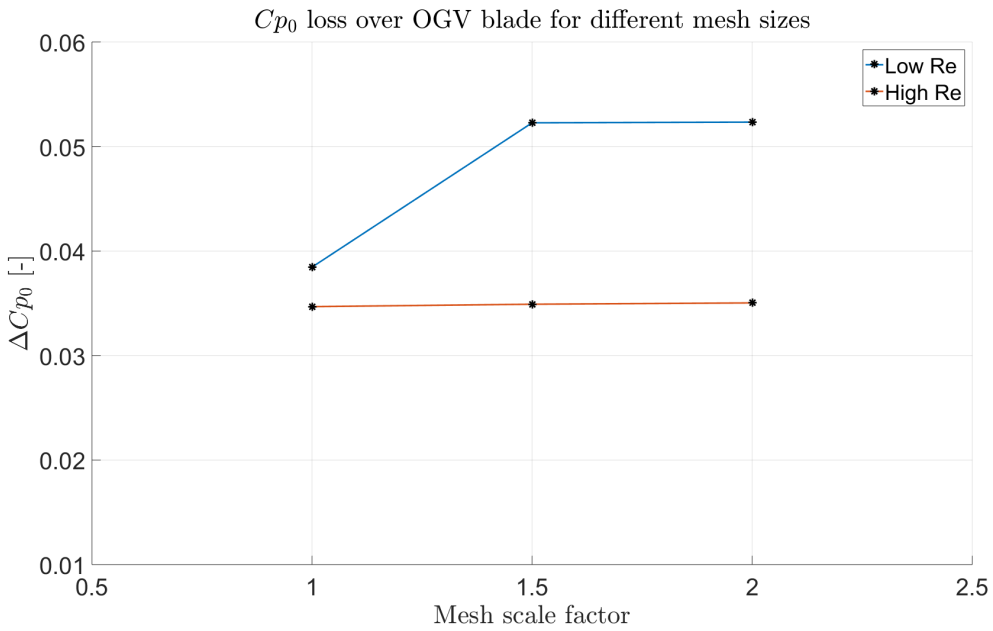

Figure 4.2: Total pressure coefficient loss over OGV blade for different meshes

Because the pressure loss between the meshes is nearly unchanged for the high Reynolds case either mesh can be chosen for the rest of the investigations.

To minimize computational time the baseline mesh was chosen to be used in all cases. However, for the low Reynolds case the change in total pressure drop is significant and it was a mistake to choose the base mesh. It would have been correct to choose the intermediate mesh for the remainder of the investigation.

Figures 4.3 - 4.5 show the wall y^+ of the OGV blade, hub and casing respectively for the low Reynolds case. The wall y^+ is close to one but on the limit of being acceptable.

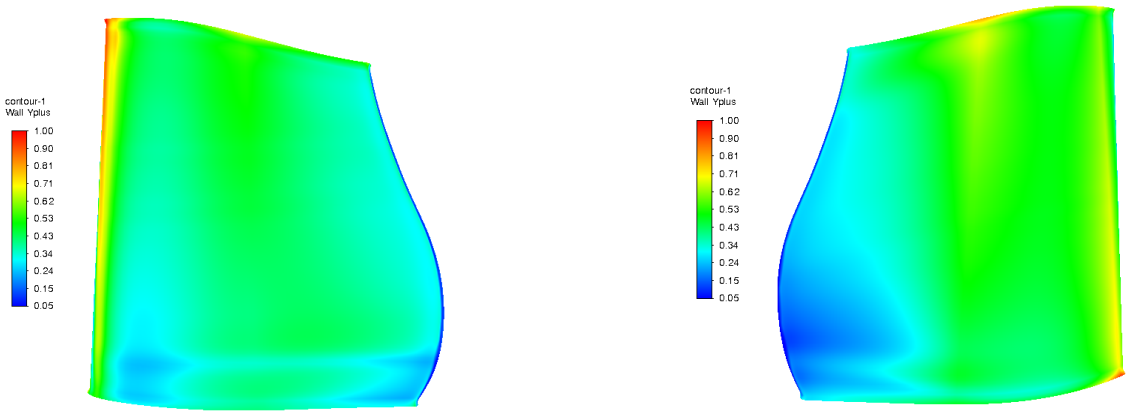

Figure 4.3: Wall y^+ of the OGV blade - Low Reynolds case

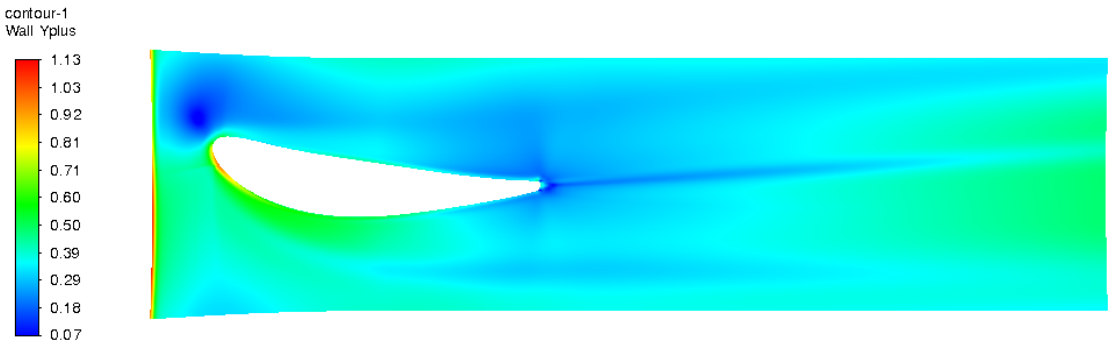

Figure 4.4: Wall y^+ of the OGV hub - Low Reynolds case

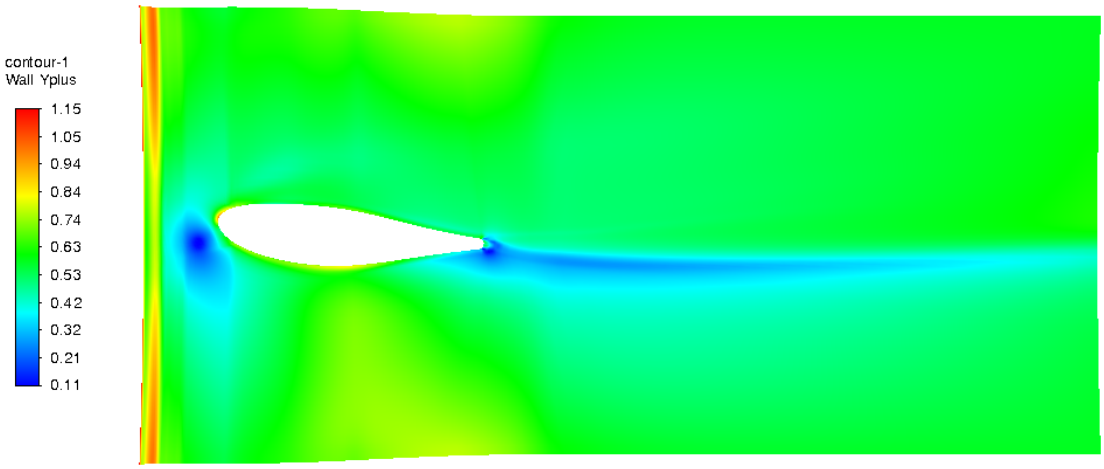

Figure 4.5: Wall y^+ of the OGV casing - Low Reynolds case

Similarly, figures 4.6 - 4.8 show the wall y^+ of the OGV blade, hub and casing respectively for the high Reynolds case. Also in this case the wall y^+ value is close to 1 in most of the domain as desired but close to the acceptable limit.

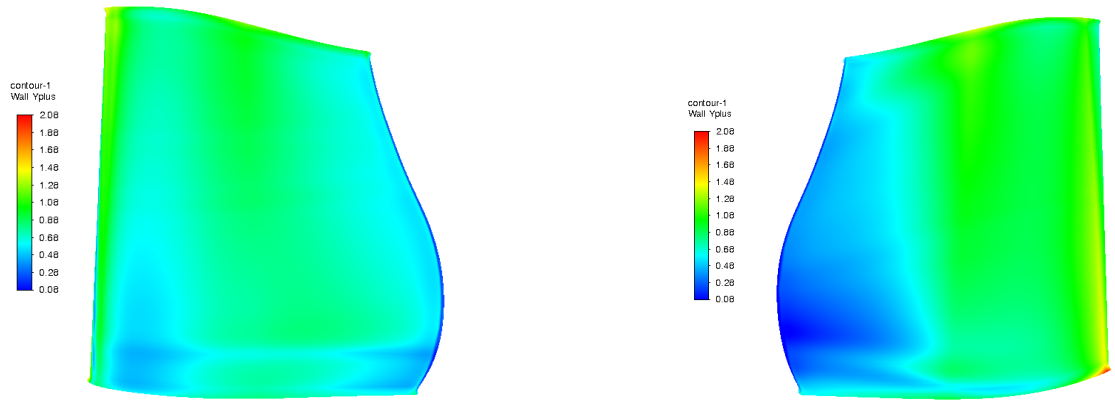

Figure 4.6: Wall y^+ of the OGV blade - High Reynolds case

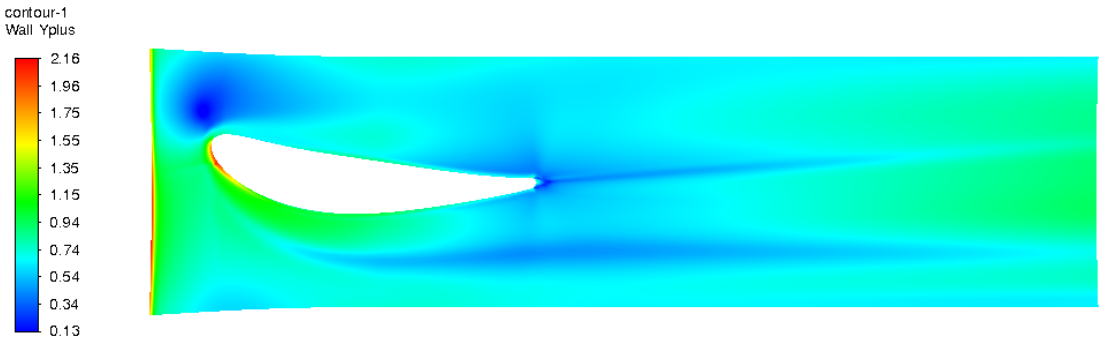

Figure 4.7: Wall y^+ of the OGV hub - High Reynolds case

Finally the base and intermediate meshes are shown for comparison in figure 4.9 and 4.10 respectively. In a future study the wall y^+ and mesh refinement should be improved. Due to time constraints further refinement of the mesh was not carried out.

4.2 Investigation of different mesh interfaces

In this section the results of the investigation of different mesh interfaces are presented.

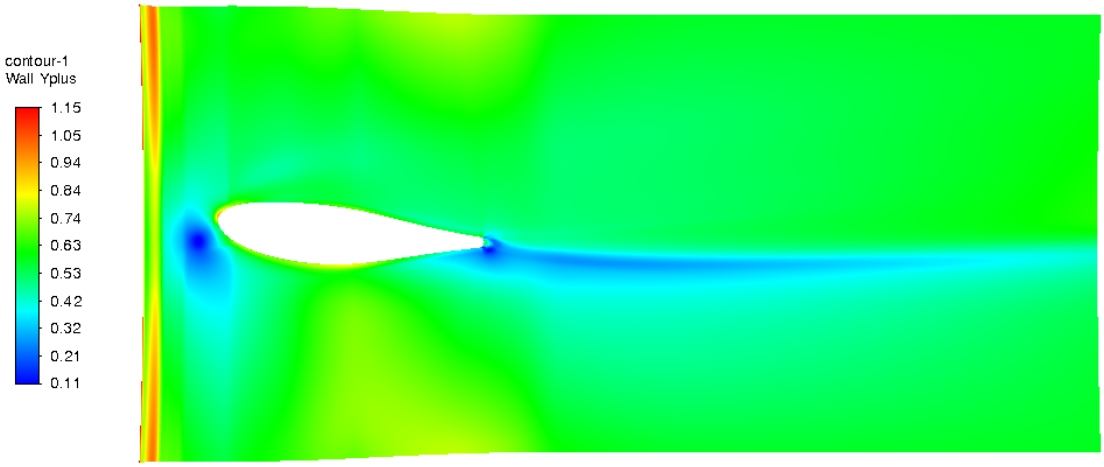

Figure 4.8: Wall y^+ of the OGV casing - High Reynolds case

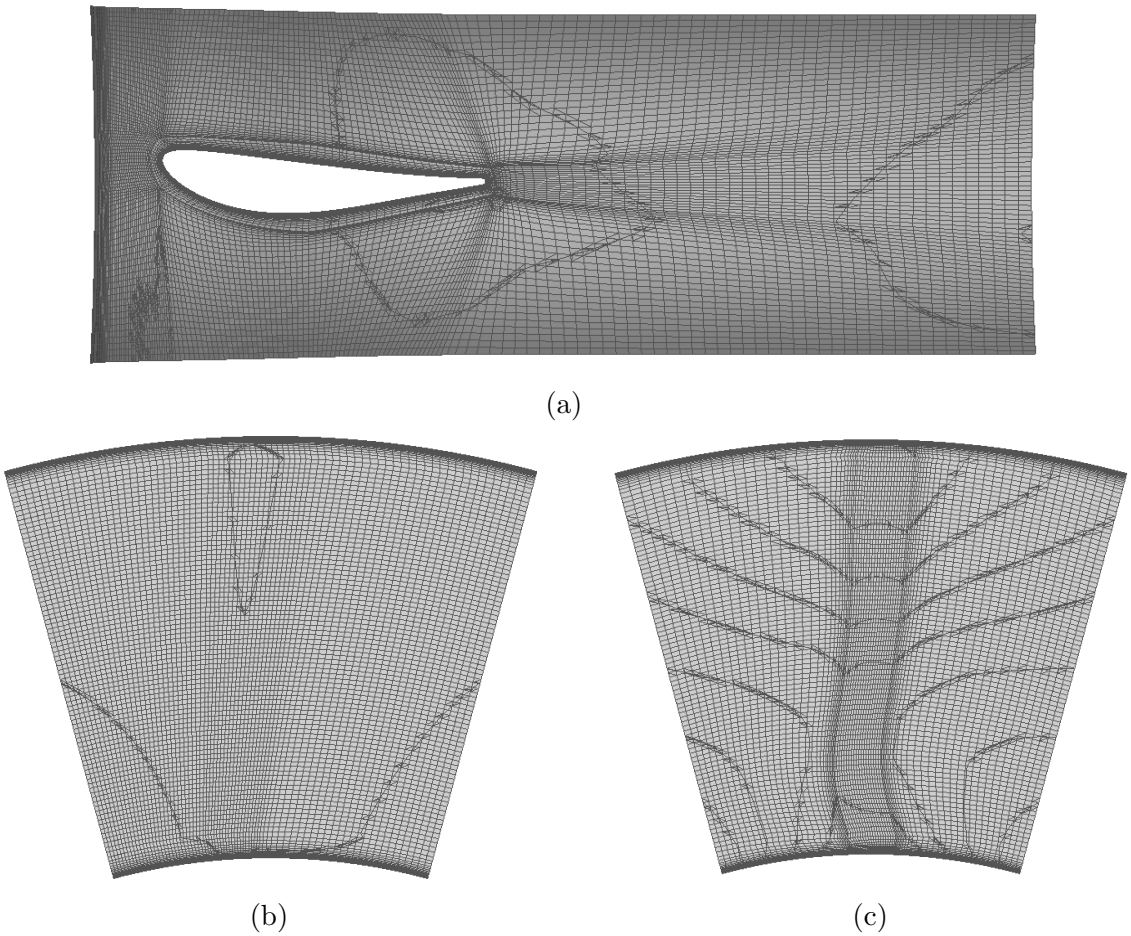

(a)

(b)

(c)

Figure 4.9: Base mesh at 50% span, US and DS measurement planes

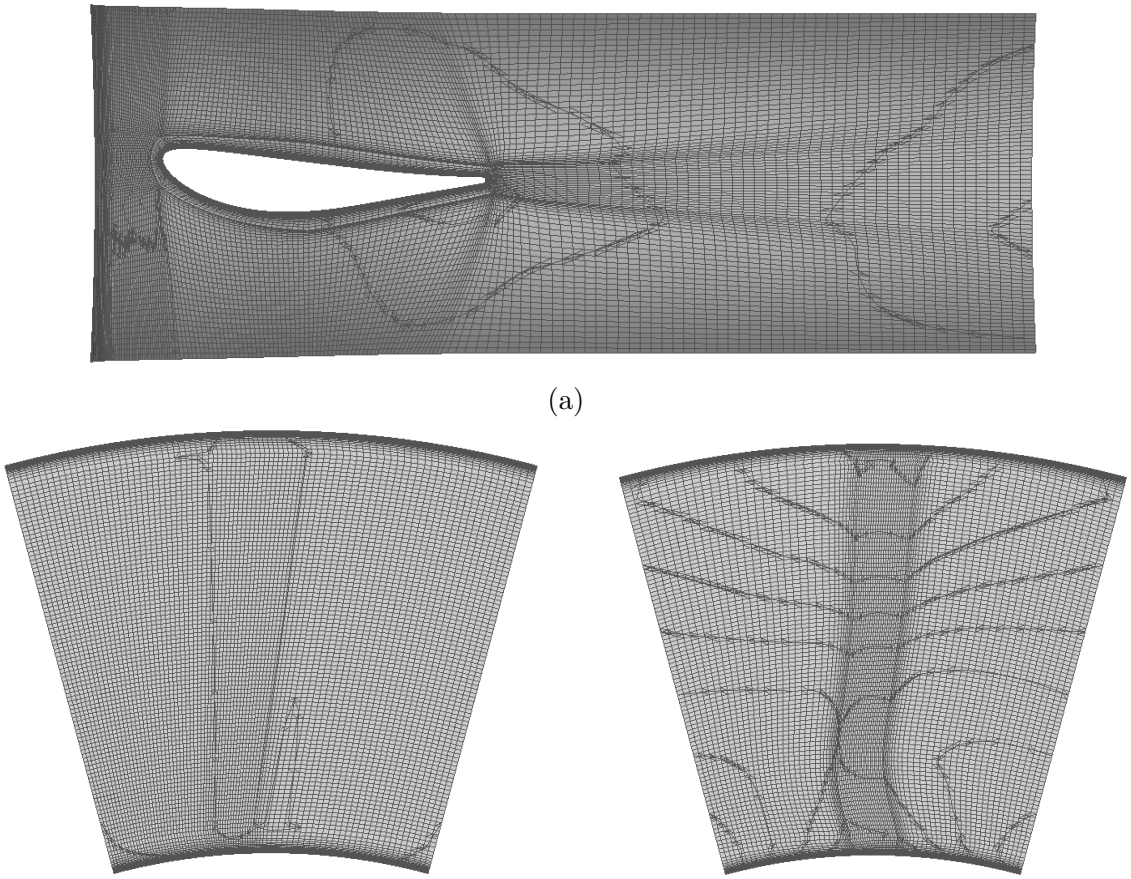

(a)

(b) (c)

Figure 4.10: Intermediate mesh at 50% span, US and DS measurement planes

4.2.1 Normal mesh interface

Test runs of the normal mesh interface resulted in wrong mass flow through the domain and no test case successfully converged. This was expected as the requirements of the normal mesh interface was not fulfilled. [6] It is observed that the normal mesh interface cannot be used as an approximation for flow through domains with non-conformal mesh interfaces. If the normal mesh interface is to be used more blades in the stator and rotor domains (5 and 6 blades respectively) must be included to yield 30° sectors resulting in conformal meshes. This would increase the number of cells in the two domains by a factor of 5 and 6, respectively, significantly increasing the required computational power.

4.2.2 Turbo interface

For the turbo interface the pitching-scale model and the turbo interface mixing plane results are presented in section 4.2.2.1 and 4.2.2.2 respectively.

4.2.2.1 Pitch-scale and no pitch-scale

When using the pitch-scale between stator and rotor and no pitch-scale between rotor and OGV the flow over the mesh interface is not mixed out as in the case of the mixing plane. Instead, wakes are transfered into the next domain as can be observed in figure 4.11. However, in the simulation 6 wakes are observed which has to come from the 6 rotors. In the experimental measurements only 5 wakes can be observed, see figure 4.12. [10] These 5 wakes trace back to the 5 stators which in reality travel through the rotor row into the TRS.

The rotor wakes would not be visible because the rotor is in constant motion and the wake of the rotor blade is traveling with the rotor blade around the axis of rotation. The rotor wakes do not have time to develop in the axial direction and are not visible in the experimental data. Therefore, the results seen using the pitching scale model are incorrect.

Due to the steady state simulation the rotor is held in one place and the fluid is rotated to model the effect of the real rotating blade row. Because the blades are standing still, the wakes travel downstream and are clearly visible in the simulation results. Especially the results in figure 4.11b compared to literature [11] and experimental results [10] are inaccurate. It is therefore advised against using the pitching scale model as it exists today when running steady state simulations. It is of interest to have another look at this option when future updates of Fluent are released.

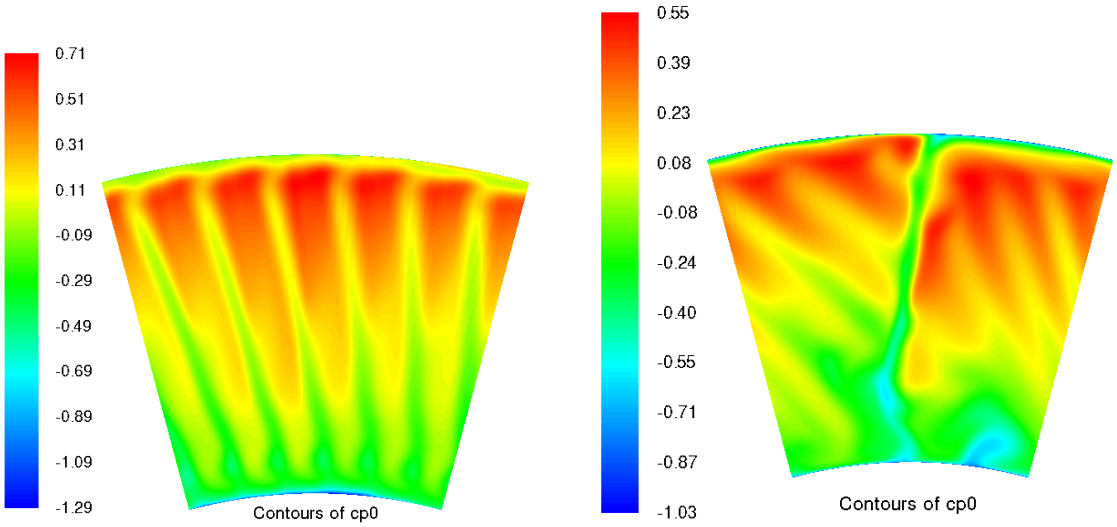

(a) Upstream of OGV (b) Downstream of OGV

Figure 4.11: Total pressure using the no pitch-scale model

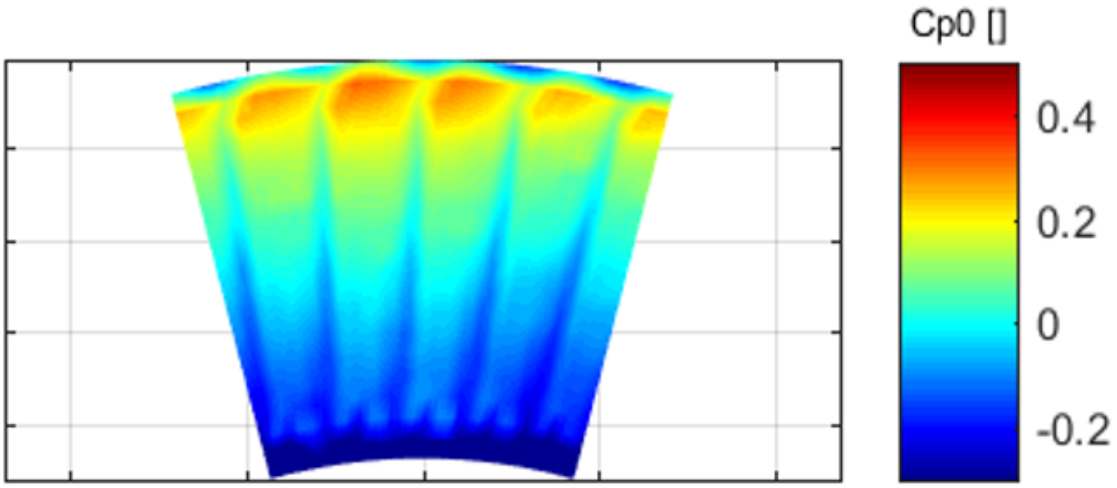

Figure 4.12: Experimental total pressure coefficient contour at US measurement plane

4.2.2.2 Turbo interface mixing plane

Because the mixing plane in the turbo interface is limited to 10 interpolation points, figure 4.13 shows how low the resolution becomes compared to a normal mixing plane with a pressure inlet boundary condition. For this reason alone it is preferable to use the normal mixing plane in this version of Fluent. The turbo interface mixing planes also use the pitching scale model regardless of the difference in pitch between the two domains which results in unreliable results. [6]

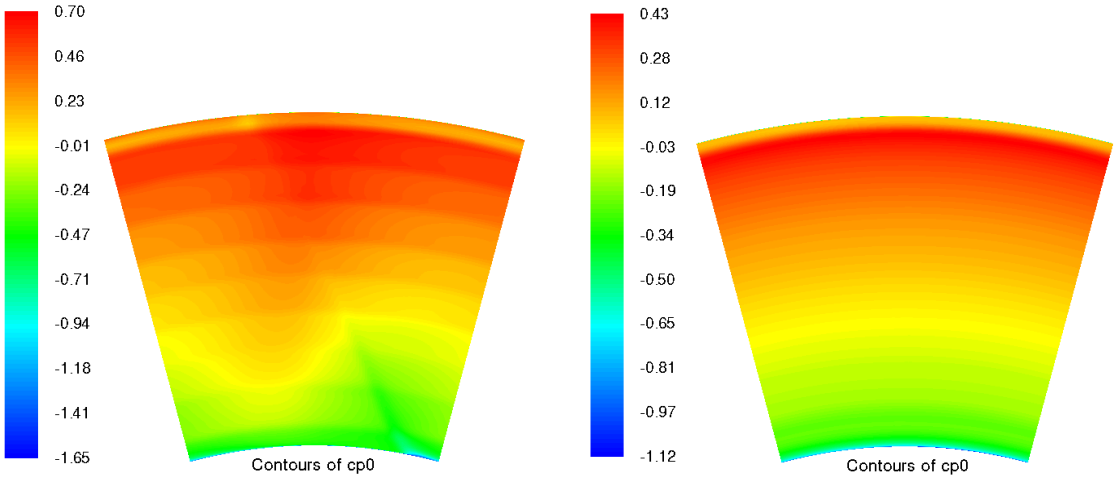

(a) Turbo interface mixing plane model (b) Normal mixing plane model

Figure 4.13: Total pressure behind rotor-OGV interface (US mesurement plane) using the different mixing plane models

4.2.3 Mixing plane

As discussed in section 4.2.2.1, running a steady state simulation of a moving rotor gives a time-frozen picture of the real flow where in a real turbine the rotor wakes would move with the rotor. Therefore, using a mixing plane to mix out the flow in steady state simulation gives a better approximation of the flow as total pressure will be preserved without the effects of the rotor wakes hitting the OGV. The total pressure contour plot of the normal mixing plane was shown in figure 4.13b.

Finally, comparison between the radially mass averaged total pressure coefficient and experimental data for the pitching-scale model, turbo interface mixing plane and a normal mixing plane with the pressure inlet boundary condition is shown in figure 4.14. It is concluded that the normal mixing plane is best suited to achieve a good approximation of the incoming flow to the OGV.

4.3 Baseline setting comparison

The results of comparing different baseline settings are presented in this section.

4.3.1 Difference in operating pressure

Comparison between different operating pressure are shown in figure 4.15 - 4.17. No significant difference is observed when changing the operating pressure. When running double precision in Fluent the difference should be insignificant, but best practice would be to set the operating pressure to 101325 Pa (close to the pressure

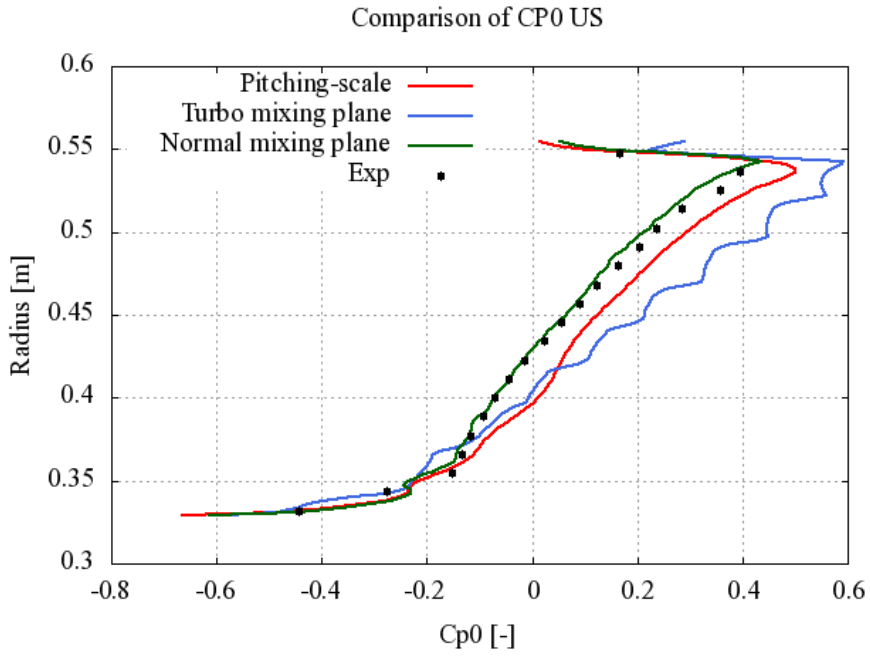

Figure 4.14: Comparison of radially mass averaged total pressure coefficient for different mesh interfaces

expected in the domain) to minimize numerical errors [6].

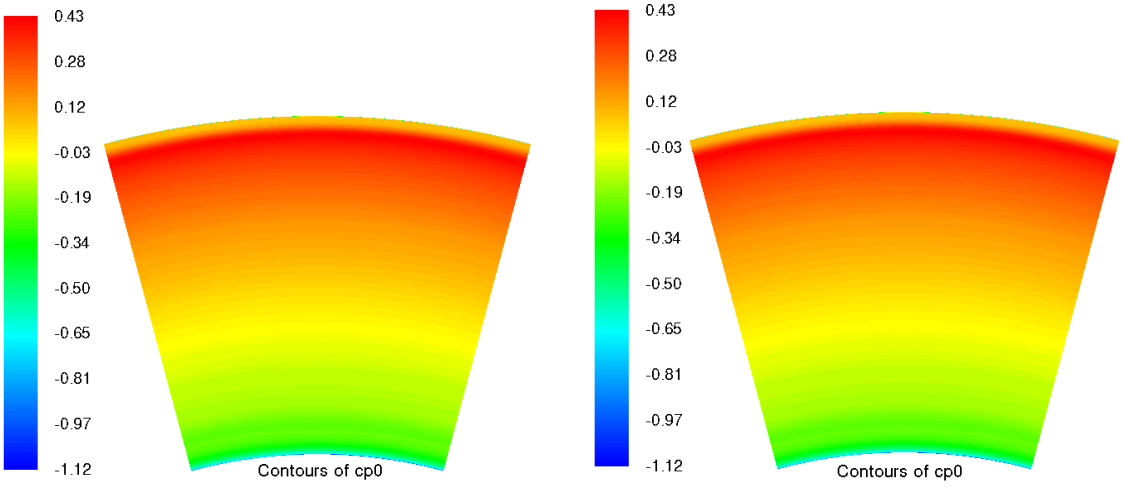

(a) OP = 0 Pa (b) OP = 101325 Pa

Figure 4.15: Difference in total pressure US for different operating pressure

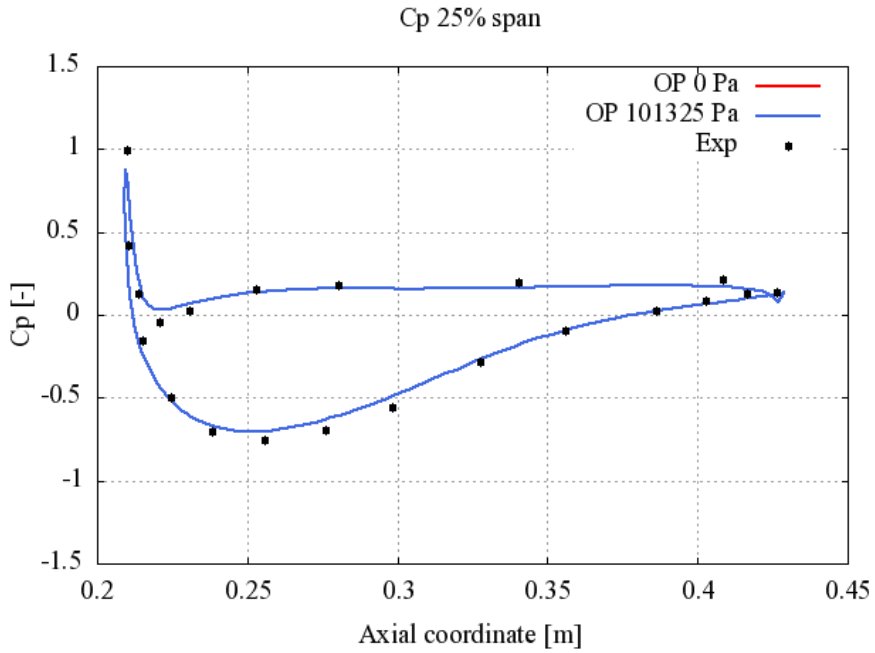

Figure 4.16: Difference in blade loading at 25% span for different operating pressures

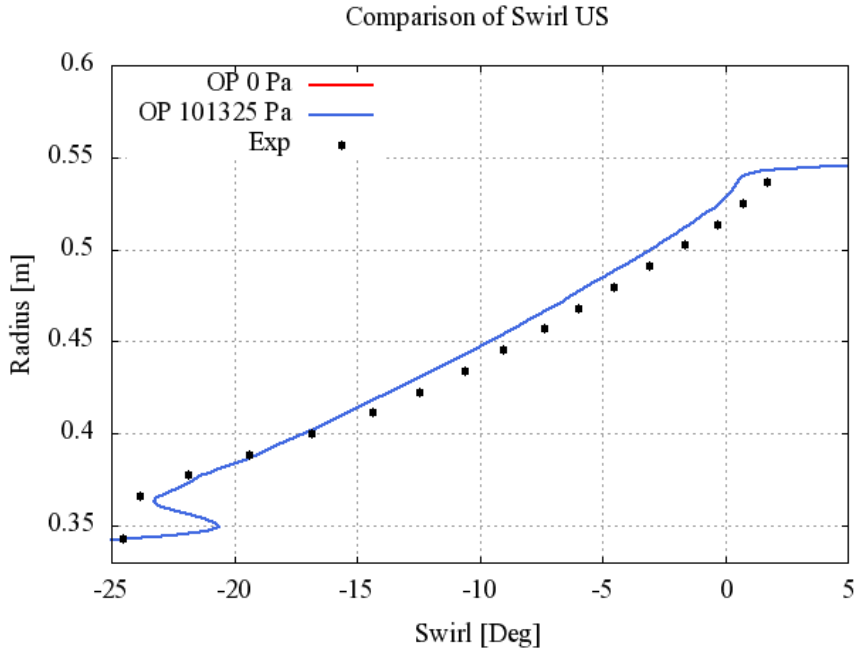

Figure 4.17: Difference in inlet swirl for different operating pressures

4.3.2 Mixing plane boundary conditions

Figure 4.18 shows the total pressure contour at the US measurement plane using the two different inlet boundary conditions for the mixing plane model. In figure 4.18a it is observed that the total pressure does not match the behavior expected from experimental data shown in figure 4.12. Features along the sides of the sector that are not visible in the experimental data exist in the mass flow inlet contours.

Instead, from the mixing plane it is preferable that the total pressure profile should be approximated by radial bands as shown in figure 4.18b. Figure 4.21 shows that the US swirl of the pressure inlet and massflow inlet is close. Regardsless, in figure 4.19 and 4.20 it is seen how the pressure inlet gives a better match of the blade loading and total pressure US respectively. The approximation achieved with the pressure inlet mixing plane is therefore chosen as the preferred setting for the remainder of the simulations.

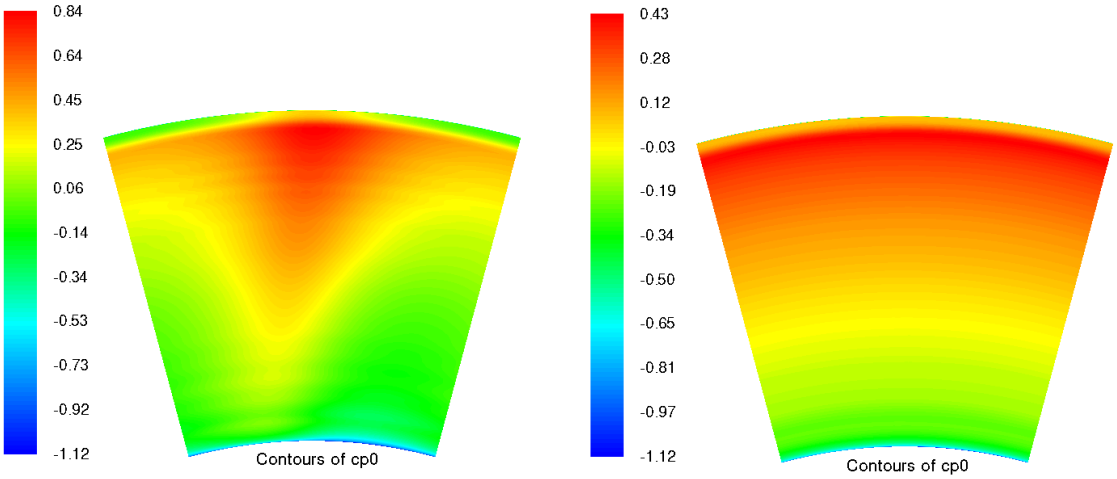

(a) Massflow inlet (b) Pressure inlet

Figure 4.18: Difference in total pressure US for different mixing plane boundary conditions

4.3.3 Difference in mixing plane under-relaxation

Figure 4.22 shows the two under-relaxation settings investigated. The default setting is 0.05. No significant difference can be observed but due to the sensitivity to reverse flow a conservative approach is recommended to avoid convergence problems. The under-relaxation can be raised as the simulation is converging if significant reverse flow is no longer present or expected. Finding a good under-relaxation value may come down to trial and error. In this study the default value of 0.05 was retained.

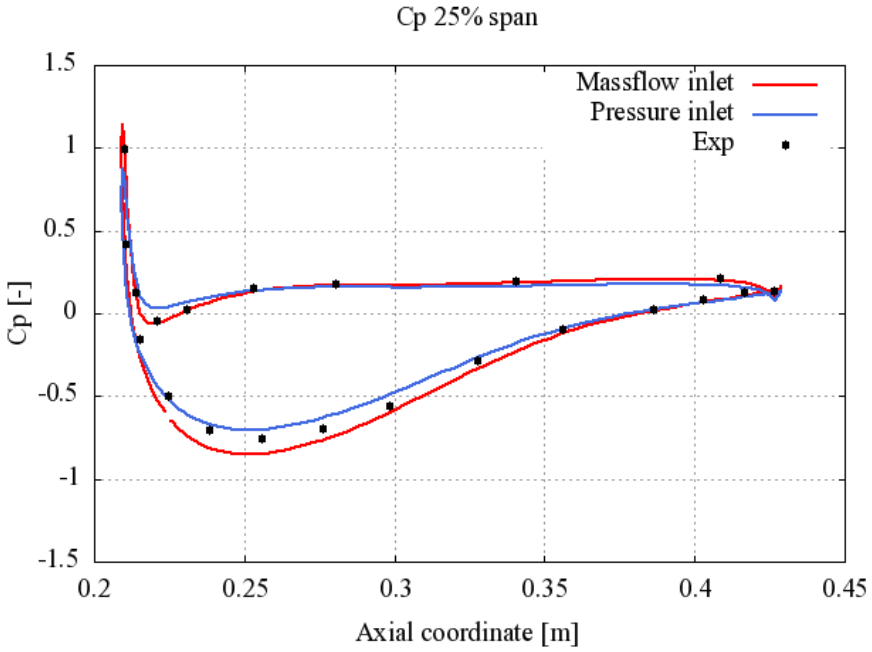

Figure 4.19: Difference in blade loading for different mixing plane boundary conditions

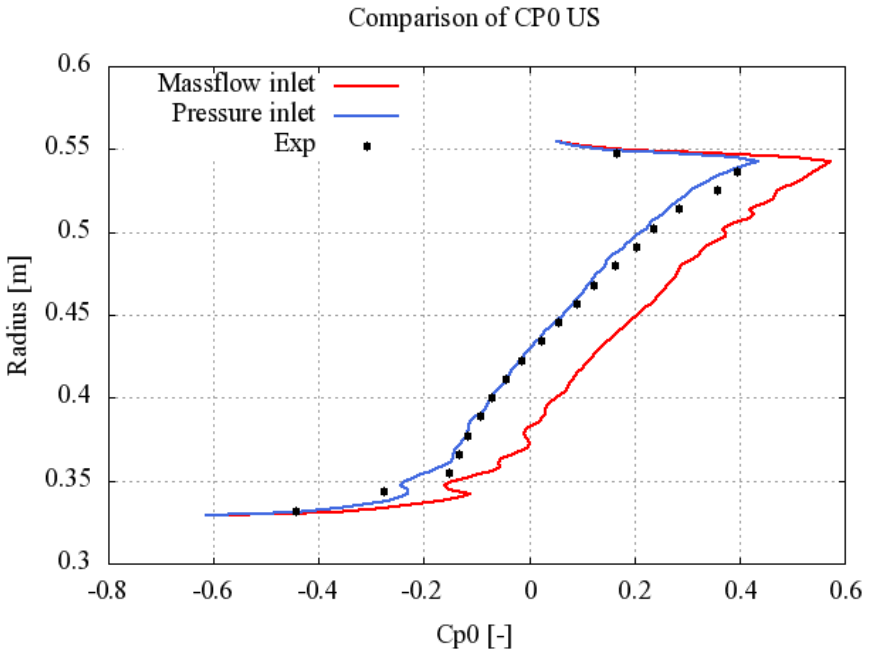

Figure 4.20: Difference in inlet total pressure coefficient for different mixing plane boundary conditions

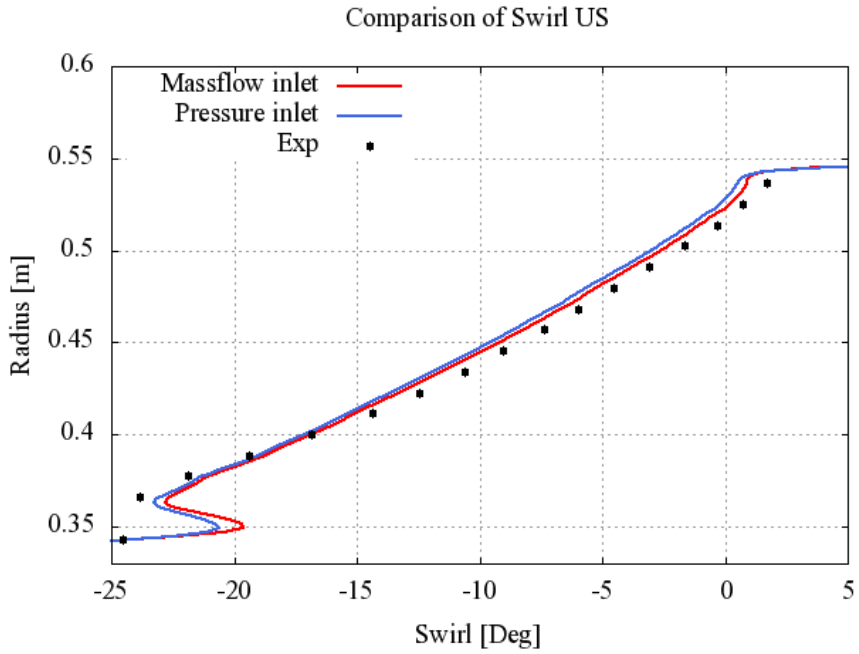

Figure 4.21: Difference in inlet swirl for different mixing plane boundary conditions

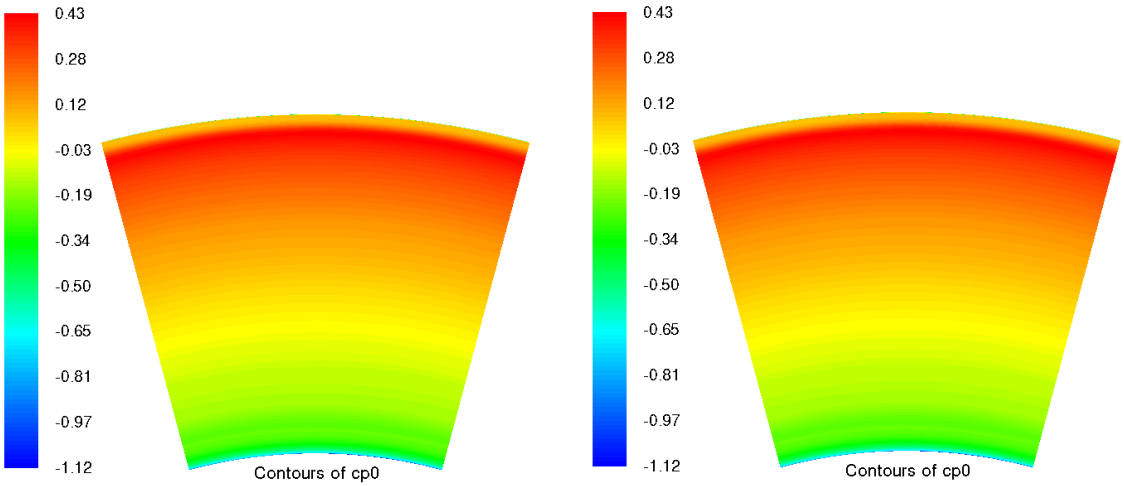

(a) Under-relaxation = 0.05 (b) Under-relaxation = 0,1

Figure 4.22: Difference in total pressure US for different under-relaxation across the mixing plane

In summary, the simulations should be performed with a operating pressure taken close to the pressure in the domain (here taken as the atmospheric pressure), with the pressure inlet boundary condition on the mixing plane and with under relaxation

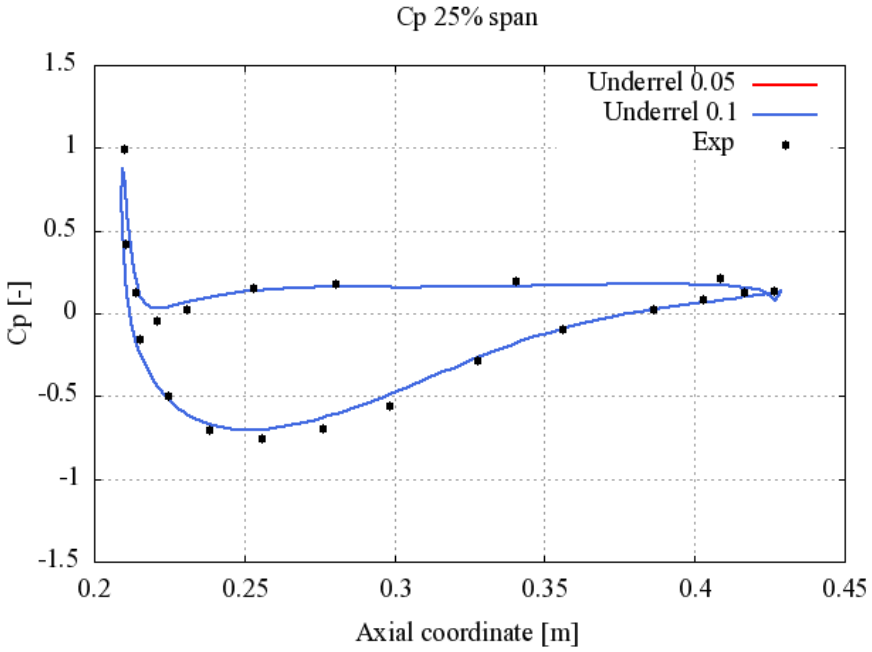

Figure 4.23: Difference in blade loading for different under-relaxation across the mixing plane

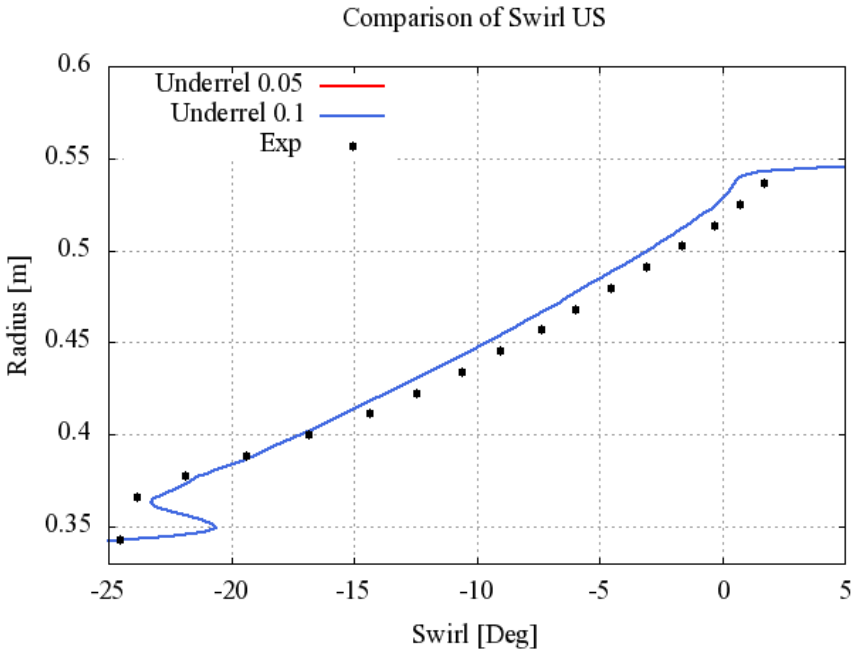

Figure 4.24: Difference in inlet swirl for different under-relaxation across the mixing plane

low enough to ensure stability (here taken as the default value 0,05).

4.4 ADP0

The results of the on-design point ADP0 steady state analysis made to compare simulation data to experimental data is presented and discussed below.

4.4.1 Low Reynolds case

The blade loading of the low Reynolds case is shown at three different spans in figure 4.25. The blade loading in closely matched by the $rk\varepsilon$ model but well approximated with all three models. Especially at higher span, some low pressure points are missed by the pressure side of the blade near the leading edge as seen in figures 4.25b and 4.25c.

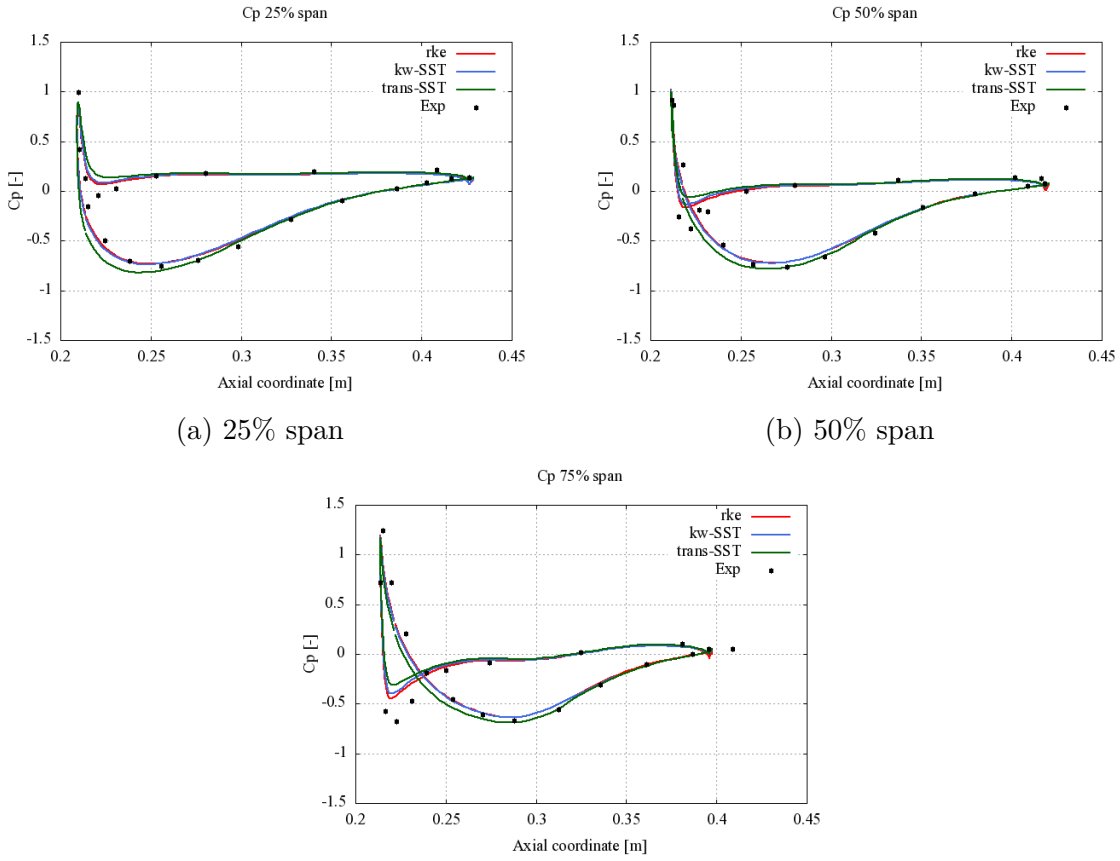

(a) 25% span

(b) 50% span

(c) 75% span

Figure 4.25: Blade loading at different spans: ADP0 low Reynolds case

Radial profiles of swirl are shown for the US and DS measurement planes in figure

4.26. The incoming swirl to the OGV is seen to be a couple of degrees off compared to the experimental data. As a result, the DS swirl is also about two degrees offset. A better matching of the swirl may results in the leading edge blade loading being better matched as well.

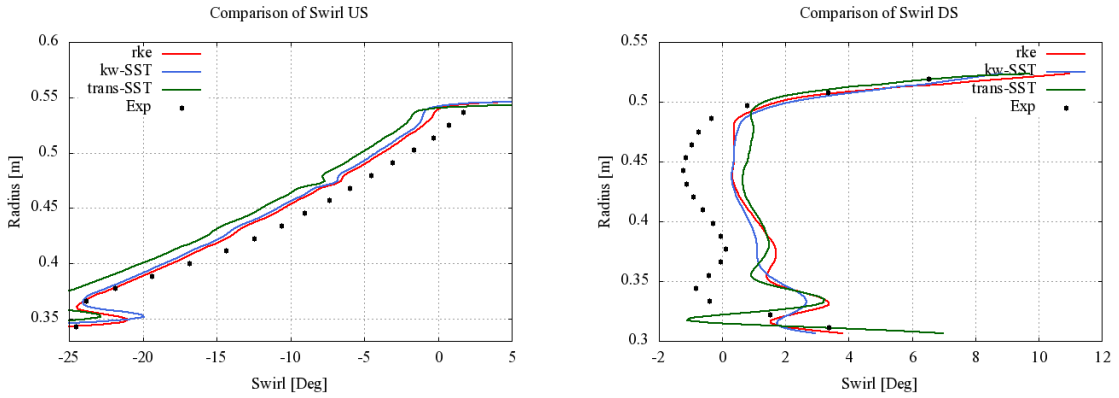

(a) US (b) DS

Figure 4.26: Swirl angle at US and DS measurement planes: ADP0 low Reynolds case

Figure 4.27 shows radial profiles of Cp_0 at the US and DS measurement planes. Because the upstream total pressure is pretty well matched the deviation in swirl is likely due to wrong rotational speed in the rotor domain rather than wrong mass-flow. Matching inlet swirl is discussed in more detail in section 4.6.

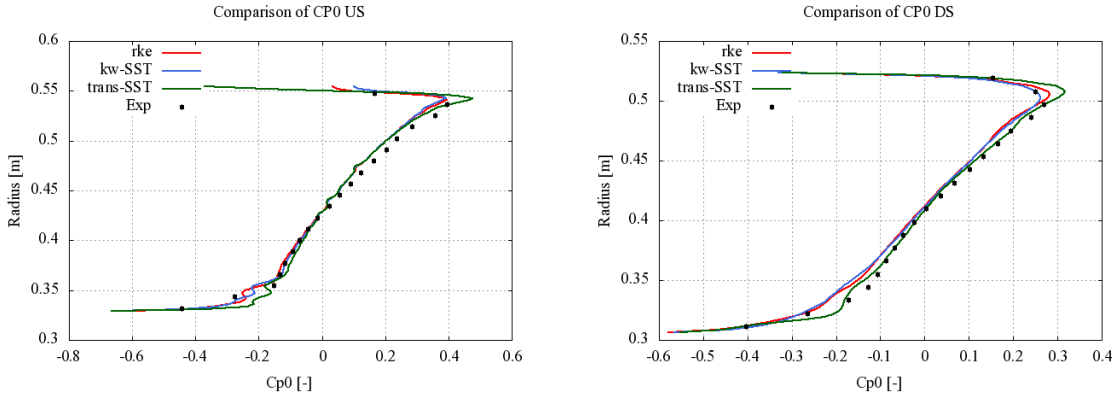

(a) US (b) DS

Figure 4.27: Total pressure coefficient at US and DS measurement planes: ADP0 low Reynolds case

A total pressure coefficient contour at the DS measurement plane is shown for all three turbulence models as well as the experimental data in figure 4.28. The behav-

ior of the wake is captured fairly well for all cases.

The low pressure region in the lower half of the wake is not as distinguished as in the experimental data and the turning S-shape of the wake is not as strong. As discussed previously, the stator wakes are vaguely visible in the experimental data but due to the mixing out at the mesh interface no such effects are visible in the simulation results.

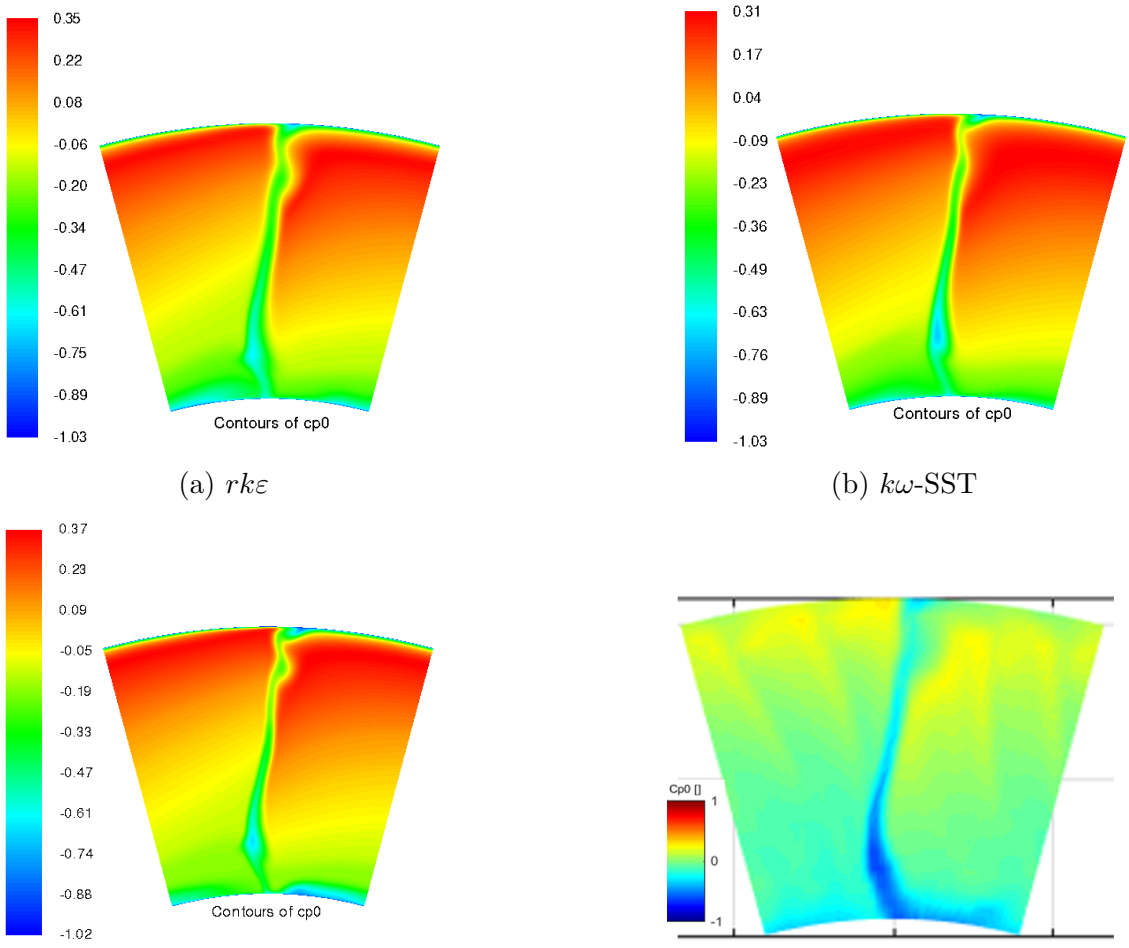

(a) $rk\varepsilon$ (b) $k\omega$-SST

(c) Transition-SST (d) Experimental

Figure 4.28: Total pressure coefficient contours at the DS measurement plane for different turbulence models: ADP0 low Reynolds case.

4.4.2 High Reynolds case

Similarly to the low Reynolds case, the blade loading at different spans for the high Reynolds case is shown in figure 4.29. Here the blade loading is better matched than in the corresponding low Reynolds case.

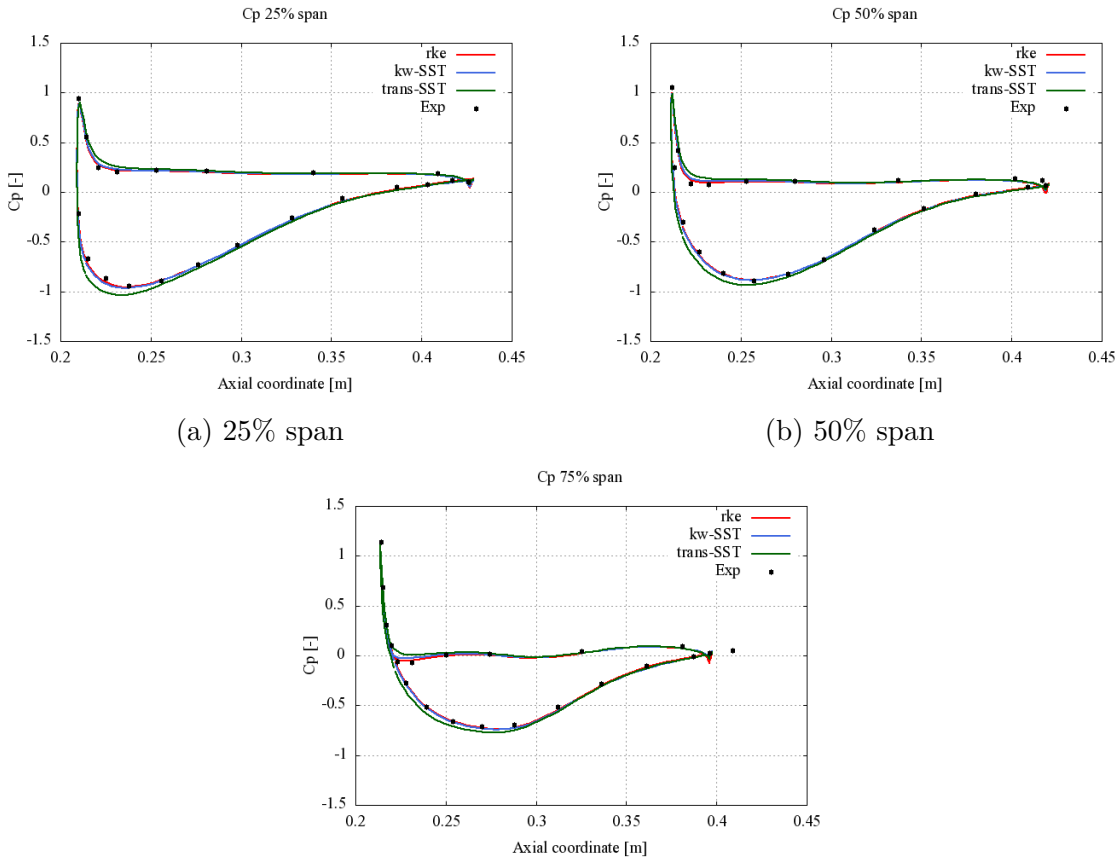

(a) 25% span

(b) 50% span

(c) 75% span

Figure 4.29: Blade loading at different spans: ADP0 high Reynolds case

Also the upstream and downstream swirl angles, shown in figure 4.30, are better matched than in the low Reynolds case. Upstream the $rk\varepsilon$ model gives the closest result.

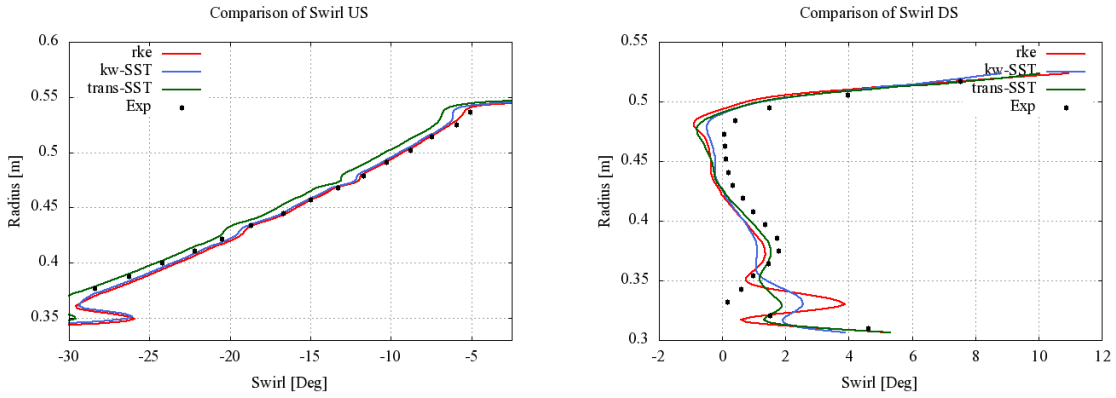

(a) US (b) DS

Figure 4.30: Swirl angle at US and DS measurement planes: ADP0 high Reynolds case

The radial profile of the total pressure coefficient in figure 4.31 is slightly overestimated at the US measurement plane but well matched in the DS measurement plane.

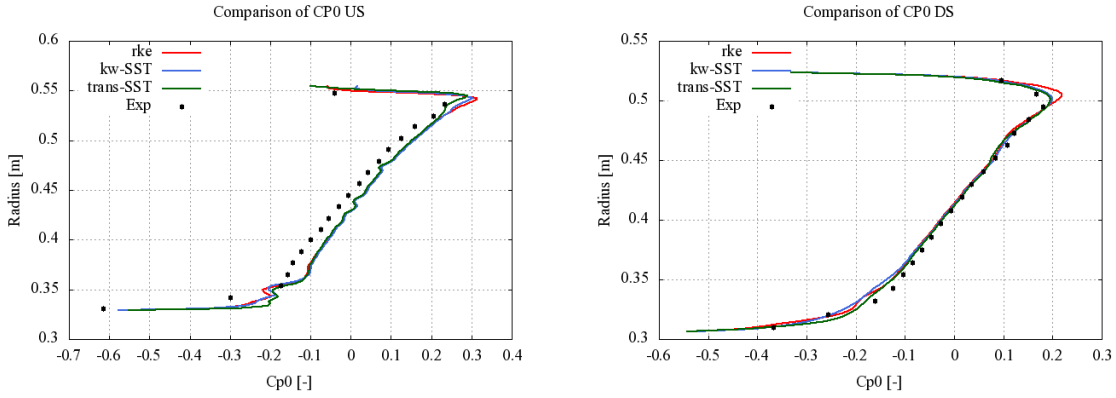

(a) US (b) DS

Figure 4.31: Total pressure coefficient at US and DS measurement planes: ADP0 high Reynolds case

Lastly the total pressure contours at the DS measurement plane are presented in figure 4.32d. The $rk\varepsilon$ contour is quite straight and underestimates the turning of the wake. The transition model matches the shape of the wake slightly better.

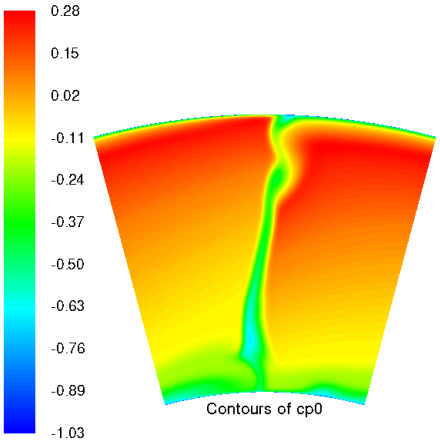

(a) $rk\varepsilon$

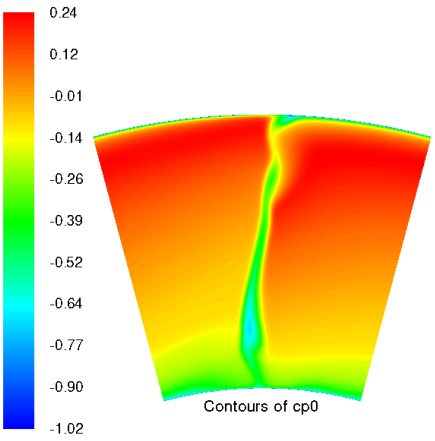

(b) $k\omega$-SST

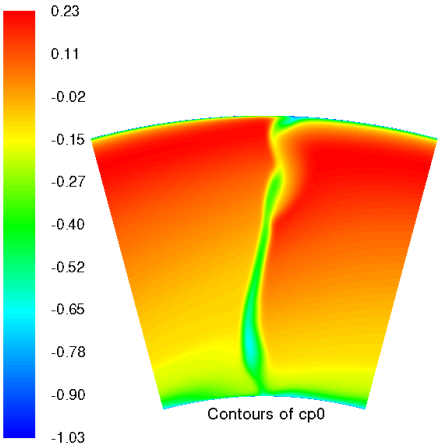

(c) Transition-SST

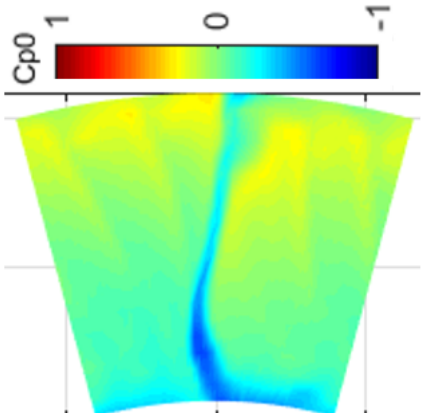

(d) Experimental

Figure 4.32: Total pressure coefficient contours at the DS measurement plane for different turbulence models: ADP0 high Reynlods case

4.5 Off-design points

When comparing the results of the off-design points to ADP0 presented above the only case with significantly different behavior observed is the ADP-10 case. In this case severe flow separation seem to occur from the OGV. Because the inlet swirl angle is high, separation is likely due to stalling of the OGV as a result of the high angle of attack. Nevertheless, a good approximation is achieved when the results are compared to the experimental data. For all other design points the behavior is similar to ADP0.

The results being as close to the experimental data as ADP0 for all off-design points suggests that the accuracy of the approximation is not significantly reduced when simulations are done for off-design conditions.

By observing these results the same conclusions are drawn for the off-design points as for the on-design point. Result figures in the same format as presented above for ADP0 are shown in Appendix I.

4.6 Adjusting rotational speed to match inlet swirl

As can be seen in some of the swirl plots at the US measurement plane the swirl angle is slightly offset from the experimental values. The actual hardware in the test facility may differ slightly from the CAD and drawing geometries due to deviations after manufacturing and assembly when the facility was built and commissioned. For example, the blade angles may differ from design values and the rotor blades may not be perfectly aligned as defined in the computational model. Therefore the inlet swirl may be affected due to hardware dissimilarities.

The swirl angle deviation seen in the low Reynolds cases can be adjusted for by changing the RPM when running simulations in Fluent. Assuming the mass flow and axial velocity stay the same a prediction was made in Microsoft excel to see how much the RPM should be changed. Figure 4.33 shows the prediction of the mass flow averaged swirl in the radial direction on the US measurement plane when the rotational speed is raised.

Running with corrected rpm the inlet swirl is better matched while blade loading remains nearly unchanged except for slightly better match close the leading edge of the OGV as shown in figure 4.34 and 4.35.

Raising the RPM is observed to make the swirl match better in these cases. If all cases have the same swirl offset it is recommended to take this into account when performing analysis in the future. The inlet swirl matching better for the high Reynolds cases may indicate that these effects are less prominent when mass flow and rotational speed is raised.

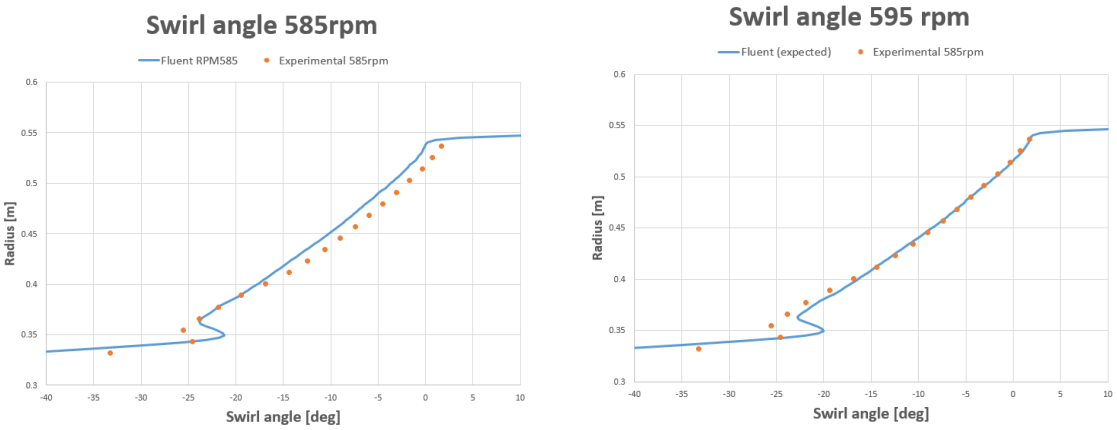

(a) Simulation data at ADP0 (b) Predicted swirl with raised rpm

Figure 4.33: Predicting inlet swirl when raising the rotational speed

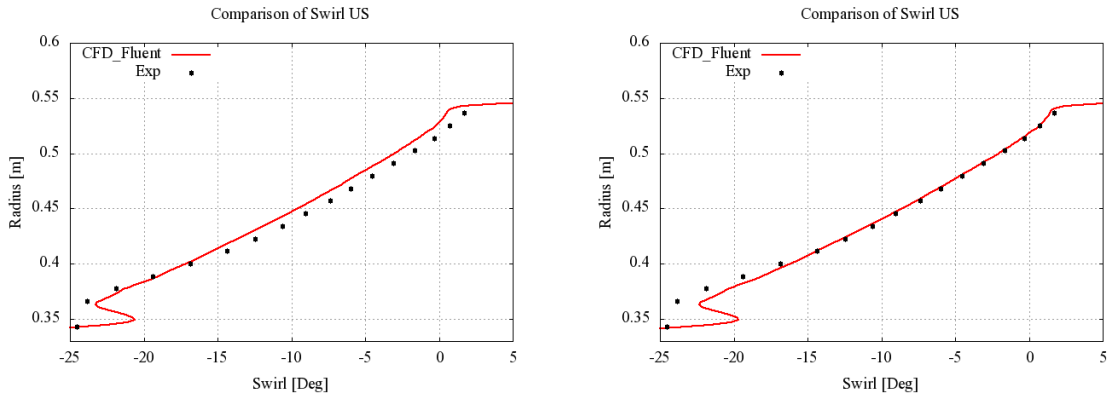

(a) Swirl not matched (b) Swirl matched

Figure 4.34: Matching inlet swirl by raising the rotational speed

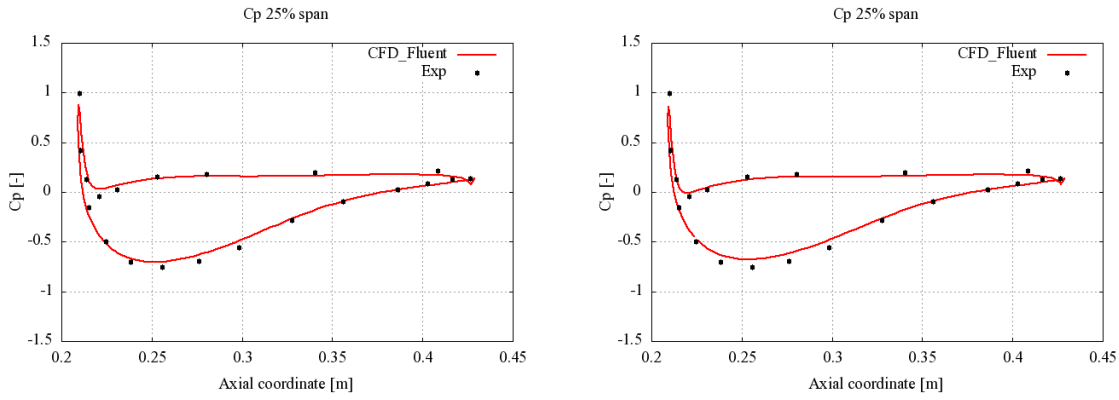

(a) Swirl not matched (b) Swirl matched

Figure 4.35: Difference in blade loading when matching inlet swirl

4.7 Convergence

Due to pre-studies leading up to the project experiencing no significant difficulty with convergence, the expectation was that none would be had during this study as well. However, this turned out not to be the case.

At an early stage, convergence was not achieved even in simple $rk\varepsilon$ cases. This is believed to have been due to faulty settings of the mesh interfaces. When the correct way of using the interface was determined, as discussed in section 4.3.2, convergence with $rk\varepsilon$ was no longer a problem and was achieved to low residual levels in all $rk\varepsilon$ cases. Because the pre-study only looked at a single mesh (the OGV without stator and rotor domains) the convergence problems with mesh interfaces was not predicted.

Convergence levels were slightly worse in $k\omega - SST$ and transition-SST. This was however expected from pre-studies that agreed well with the results in this thesis. Convergence for the transition-SST case was especially challenging, possibly due to the use of transition-SST in the whole domain.

The mixing plane model has several options for how the circumferential averaging is performed. The simplest one is area averaging and the one with highest fidelity is "mixed out" averaging. In all $rk\varepsilon$ and $k\omega - SST$ cases mixed out averaging was used. However, in the transition-SST case convergence was not achieved without changing to area averaging.

During simulations the quantities p_s, p_0, v_x and $\dot{m}$ were monitored at the DS measurement plane. The transition-SST results are considered to be trustworthy as the acceptably low residuals are accompanied by the above mentioned quantities converging to a couple of decimal places in all cases.

4.8 Heat Transfer

Figure 4.36 shows the total temperature profiles at the US measurement plane for both the low and high Reynolds cases.

Because the total temperature is almost constant over the inlet plane in both cases the inlet boundary is left unchanged and a wall temperature of $287 \pm 20K$ is added to all walls in the OGV region.

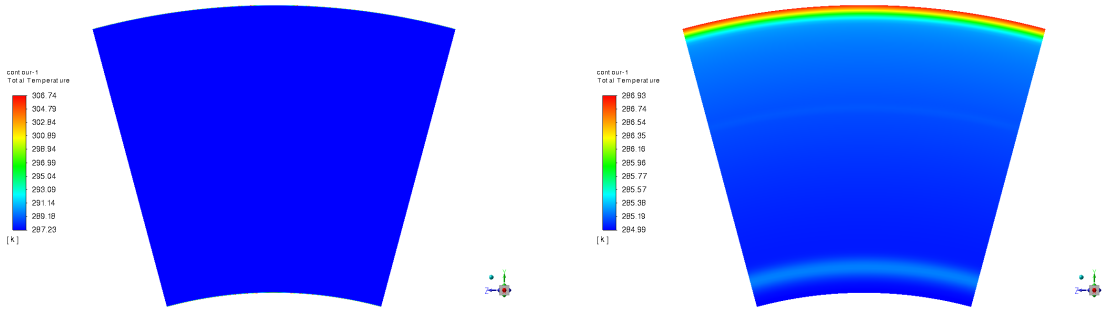

(a) Low Re case (b) High Re case

Figure 4.36: Total temperature profiles at the US measurement plane

4.8.1 Low Reynolds case

Comparing the HTC for the two cases ($\Delta T = \pm 20K$) in figure 4.37 shows that both the plus and minus case yields close to the same results. It is therefore sufficient to only consider the case with positive temperature change.

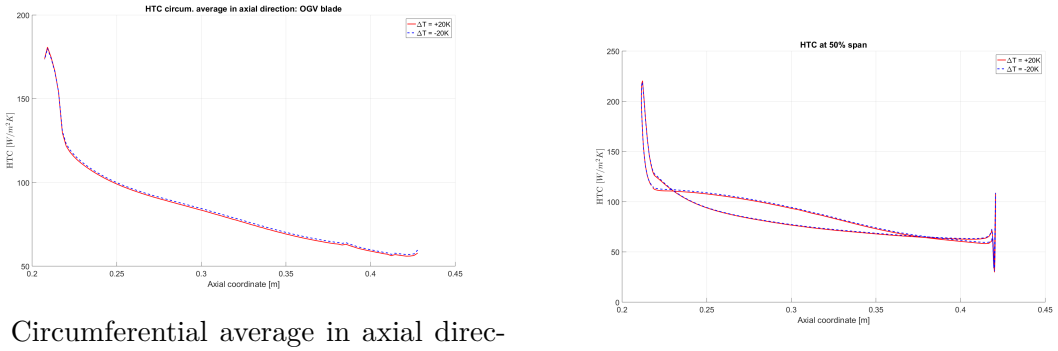

(a) Circumferential average in axial direction of OGV (b) HTC around blade at 50% span

Figure 4.37: Comparison of HTC for $\Delta T = +20K$

Figure 4.38 shows contours of the HTC on the OGV blade for $\Delta T = +20K$ low Reynolds case. The maximum heat flux is reached in the stagnating region at the OGV leading edge. Along the first part of the blade sides, the HTC is about half the value in the stagnation point. Slightly further along the blade the heat-flux rapidly drops. This is illustrated by the transition to the blue regions and is likely due to the flow transitioning from laminar to turbulent on the OGV.

The transition occurs at different axial chord locations for different spans. For example, at about 10% span the transition takes place almost immediately following the leading edge whereas at about 80% span the transition is prolonged until about 1/4 of the axial chord. At 90% span a streak that does not appear to transition is observed in figure 4.38b. Due to the tip leakage effect from the rotor shroud affecting the inlet swirl and vorticity distribution [11] this could possibly be traced back to the rotor.

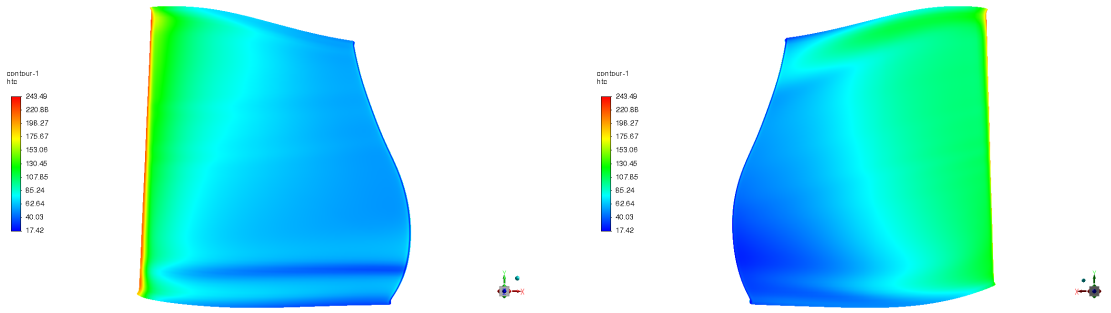

(a) (b)

Figure 4.38: HTC on OGV blade surface for $\Delta T = +20K$

In figure 4.38a a dark blue streak of low HTC is observed at about 10-20% span. The complex horseshoe vortex system manifesting might be the reason for the lower heat-flux along that part of the blade. The secondary flow effects near the hub was observed to be confined below 20% span in [11].

Similar behavior as in figure 4.38 is observed for $\Delta T = -20K$ illustrated by HTC contours on the OGV in figure 4.39. This is expected as the heat transfer should be equal with opposite sign for the $\Delta T = -20K$ case.

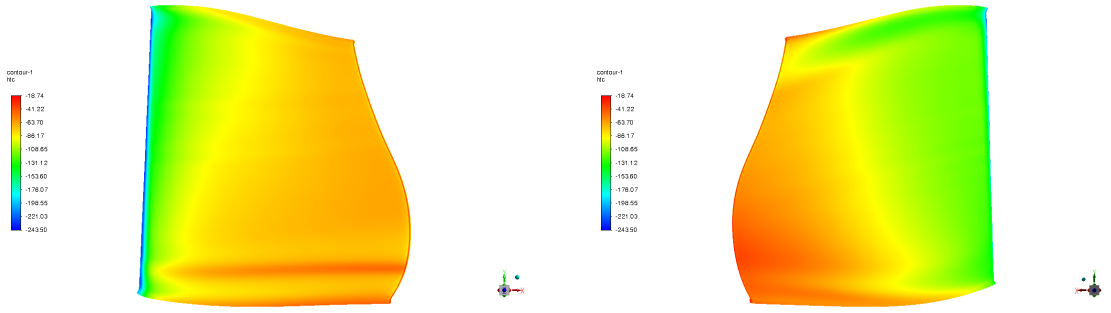

(a) (b)

Figure 4.39: HTC on OGV blade surface for $\Delta T = -20K$

The only test data currently available is HTC measurement on the OGV for the low Reynolds case. A comparison between the different turbulence models and the measured HTC is shown in figure 4.40 for the pressure side and suction side respectively. The transition model approximates the behavior of the measured HTC. The location of transition agrees well on the pressure side of the OGV but the HTC is underestimated. On the suction side the opposite is observed – the HTC is closer in magnitude but the transition point occurs too early in the CFD model.

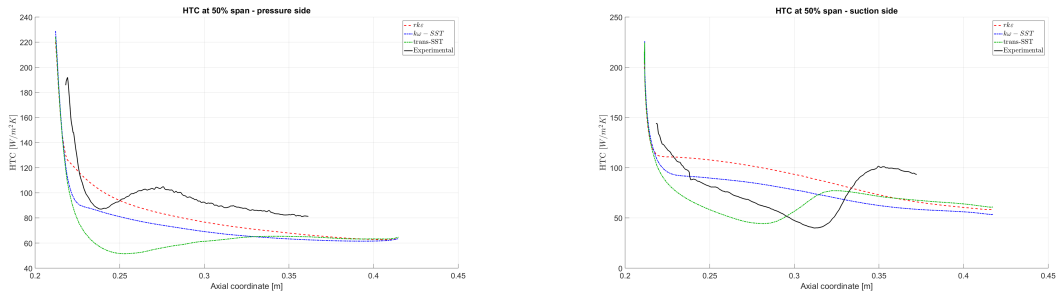

(a) (b)

Figure 4.40: HTC for different turbulence models at 50% span compared to test data

4.8.2 High Reynolds case

Similarly to the low Reynolds case, comparing the HTC for the two cases $\Delta T = \pm 20K$ in figure 4.41 shows that both the plus and minus case yields close to the same results.

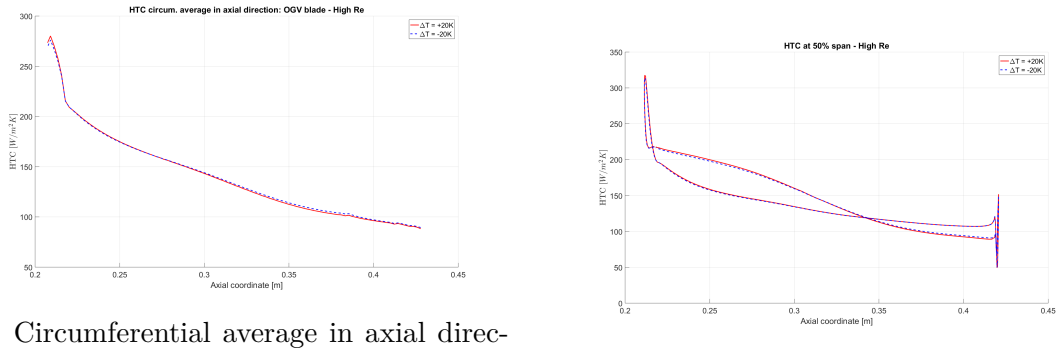

(a) Circumferential average in axial direction of OGV

(b) HTC around blade at 50% span

Figure 4.41: Comparison of HTC for $\Delta T = +20K$

No measurement data of HTC was available for the high Reynolds case. The numerical results are however shown as HTC contours in figures 4.42 - 4.43

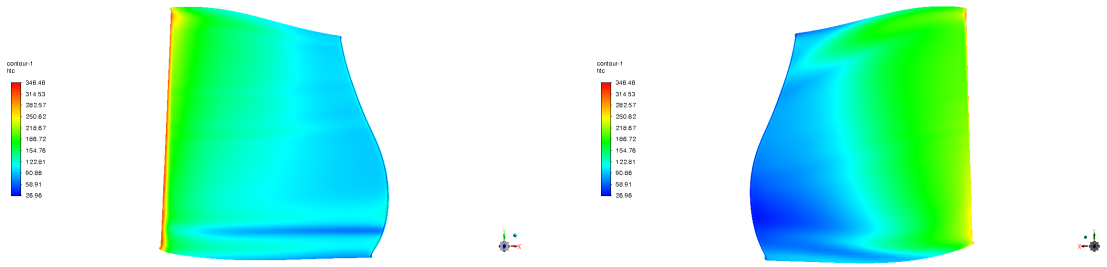

(a) (b)

Figure 4.42: HTC on OGV blade surface for $\Delta T = +20K$

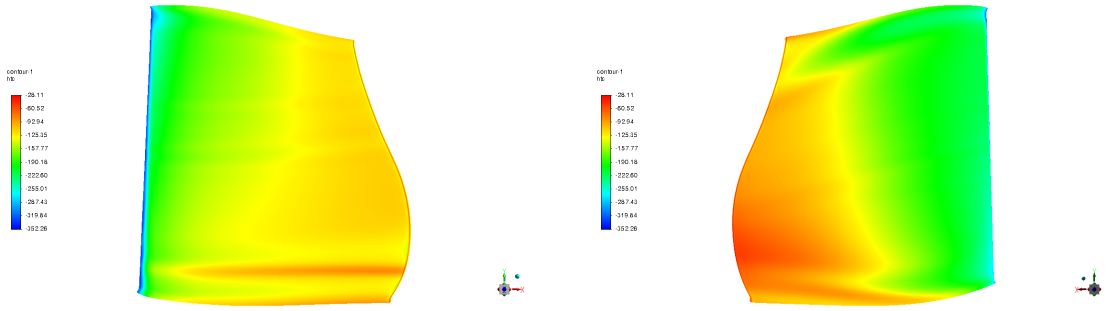

(a) (b)

Figure 4.43: HTC on OGV blade surface for $\Delta T = -20K$

5
Conclusion

In this study an investigation of the aerodynamic steady state analysis used in the design of a TRS was made. The steady state analysis was shown to be able to approximate experimental results for both design and off-design conditions using the methods outlined in this thesis.

To achieve a good approximation with a steady state analysis using several meshes it is recommended to use the mixing plane model with a pressure inlet boundary condition. The massflow inlet at the mixing plane ensures conservation of massflow but was shown to give inaccurate inlet total pressure conditions for the OGV. The under-relaxation factor of the mixing plane and the operational pressure in the domain had no significant impact on the results for the settings tested in this study.

Because of the mixing plane being sensitive to backflow, convergence can be affected if care is not taken to the placement of the mesh interfaces. When creating the computational domain, avoid mesh interfaces too close to any recirculation regions (e.g the near trailing edge of the blades) if possible. The recommended settings are summarized in table 5.1.

There are more settings available for the mixing plane model that were only briefly tested in this study. A proper investigation of these would be interesting in a future study.

The prediction model can be adjusted to compensate for offset inlet swirl distribution by changing the rotational speed in the rotor domain.

Finally, although giving an acceptable approximation, the convergence for the $k\omega - SST$ and $transition - SST$ models can be improved to be in line with the $rk\varepsilon$ model. The $transition - SST$ model when using the stator, rotor and OGV domains poses a challenge to predict the OGV inlet boundary conditions.

With that said it should be noted that all simulations are run with the same turbulence model in all three regions. Therefore, a different turbulence model will likely produce different inlet conditions to the OGV. No setting to run different turbulence models in different regions were found in Fluent. It might be interesting to analyze the stator and rotor regions without the OGV region using the turbulence model that produces the best match at the US measurement plane first. The results at the

Setting	**Recommended choice**	**Comment**
Reference frames	Stator: Stationary Rotor: Rotating OGV: Stationary	
Operational pressure	Close to expected pressure in domain	Insignificant for double precision but best practice
Mesh interface position	Away from recirculating flow	If possible
Mesh interface	Mixing plane model	
Mixing plane settings	**Recommended choice**	**Comment**
Interface boundary condition	Pressure inlet	Conserves total pressure
Under-relaxation	0.05 (Default)	Investigate if higher under-relaxation can speed up convergence
Averaging method	Mixed-out	Change to area-averaging if not converging

Table 5.1: Summary of recommended settings

rotor exit could then be exported as boundary profiles and set as inlet boundary condition to the OGV domain only running simulations with a different turbulence model.

For example, $rk\varepsilon$ could be used in the stator and rotor regions to generate the OGV inlet boundary condition followed by a transition-SST simulation of the OGV region only.

5.1 Recommended future work

Some suggestions for future work is to

- Investigate effect of changing the mixing plane model settings not thoroughly studied in this report
- Investigate any improvements in the BETA features of the pitching scale model or mixing plane within the turbo interface when they become fully implemented
- Investigate ways to improve and speed up convergence
- Run the stator and rotor regions together with $rk\varepsilon$ and export the outlet data profile. Import the profile as inlet to the OGV and run that with transition modeling.

Bibliography

[1] F. M. White, *Fluid Mechanics*, 7th ed. New York, US: McGraw-Hill Education, 2011, ISBN: 978-007-131121-2.

[2] J. D. Anderson, *Introduction to Flight*, 7th ed. New York, US: McGraw-Hill Education, 2012, ISBN: 978-007-108605-9.

[3] L. Davidson, *Fluid mechanics, turbulent flow and turbulence modeling*. 2019, Div. of Fluid Dynamics, Dept. of Mechanics and Maritime Sciences, Chalmers University of Technology, Gothenburg.

[4] L. Davidson, *An introduction to turbulence models*. 1997, Technical Report 97/2. Dept. of Thermo and Fluid Dynamics, Chalmers University of Technology, Gothenburg.

[5] A. Inc, *Ansys fluent website*, 2019. [Online]. Available: `https://www.ansys.com/products/fluids/ansys-fluent`.

[6] A. Inc, *Ansys fluent manual*, 2019.

[7] S. Dixon and C. Hall, *Fluid Mechanics and Thermodynamics of Turbomachienery*, 7th ed. Oxford, UK: Butterworth-Heinemann, 2014, ISBN: 978-0-12-415954-9.

[8] H. Saravanamuttoo *et al.*, *Gas Turbine Theory*, 7th ed. Harlow, UK: Pearson Education Limited, 2017, ISBN: 9781-292-09309-3.

[9] P. Whitney, *Pratt & whitney product and services website*, Fetched on 2019-05-21. [Online]. Available: `https://www.pw.utc.com/products-and-services/products/commercial-engines/GP7200-Engine/`.

[10] B. M. Rojo Perez, *Aerothermal Experimental Investigation of LPT-OGVs*. 2017.

[11] T. Selic *et al.*, "Aerodynamic effects of an unshrouded low pressure turbine on a low aspect ratio exit guide vane", *Proceedings of ASMe Turbo Expo 2012*, 2012.

[12] V. Perdichizzi A. Dosena, “Incidence angle and pitch-chord effects on secondary flows downstream of a turbine cascade”, *The American Society of Mechanical Engineers*, 1992.

A

Appendix I - Off-design steady state analysis results

Appendix I contains the results of the off-design points ADP+5, ADP+10 and ADP-10 from the steady state analysis.

ADP+5

This section presents the results of the off-design point ADP+5.

Low Reynolds case

The blade loading of the off-design condition low Reynolds ADP+5 is shown in figure A.1. It is observed that also for an off-design condition the blade loading is well matched. The $rk\varepsilon$ gives a slightly closer match than the $k\omega - SST$ model.

Looking at the radial profiles of US and DS swirl in figure A.2 the results are similar to those observed in the low Reynolds ADP0 case. The $rk\varepsilon$ model gives the closest match upstream but all three models are about 2 degrees off downstream.

The radial profiles of total pressure coefficient in figure A.3 show a small overestimation upstream and a fairly close match downstream.

For the total pressure contours at the DS measurement plane in figure A.4 the $k\omega - SST$ model deviates the most from the wake shape. The magnitude and shape of the $rk\varepsilon$ case is a good approximation.

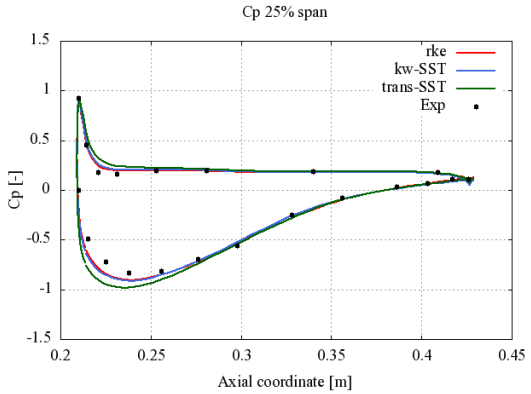

(a) 25% span

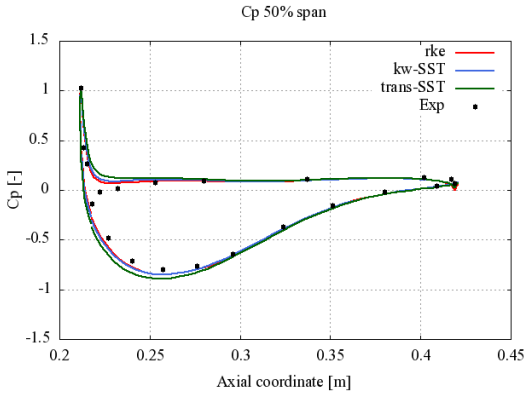

(b) 50% span

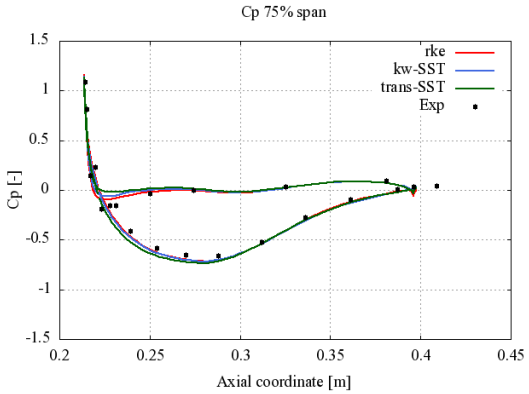

(c) 75% span

Figure A.1: Blade loading at different spans: ADP+5 low Reynolds case

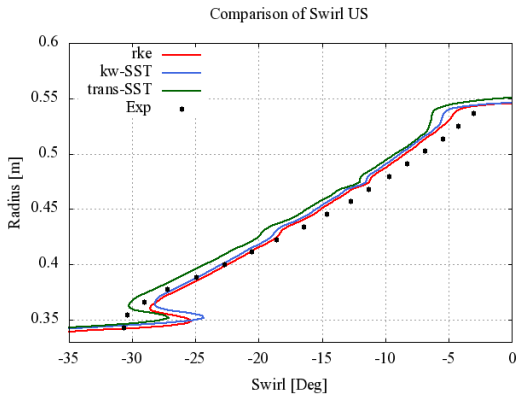

(a) US

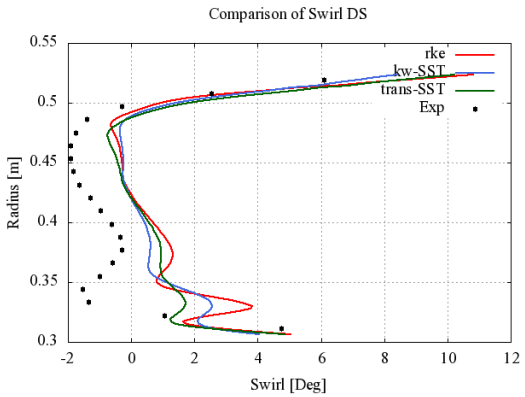

(b) DS

Figure A.2: Swirl angle at US and DS measurement planes: ADP+5 low Reynolds case

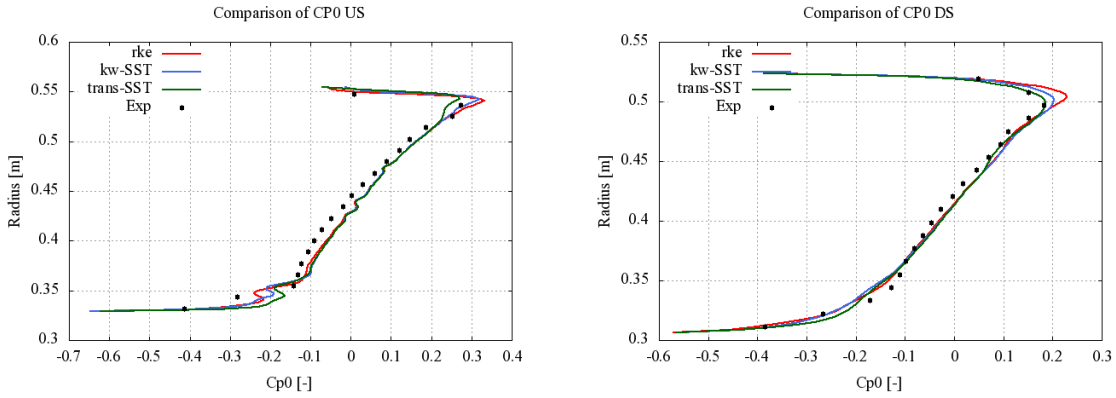

(a) US (b) DS

Figure A.3: Total pressure coefficient at US and DS measurement planes: ADP+5 low Reynolds case

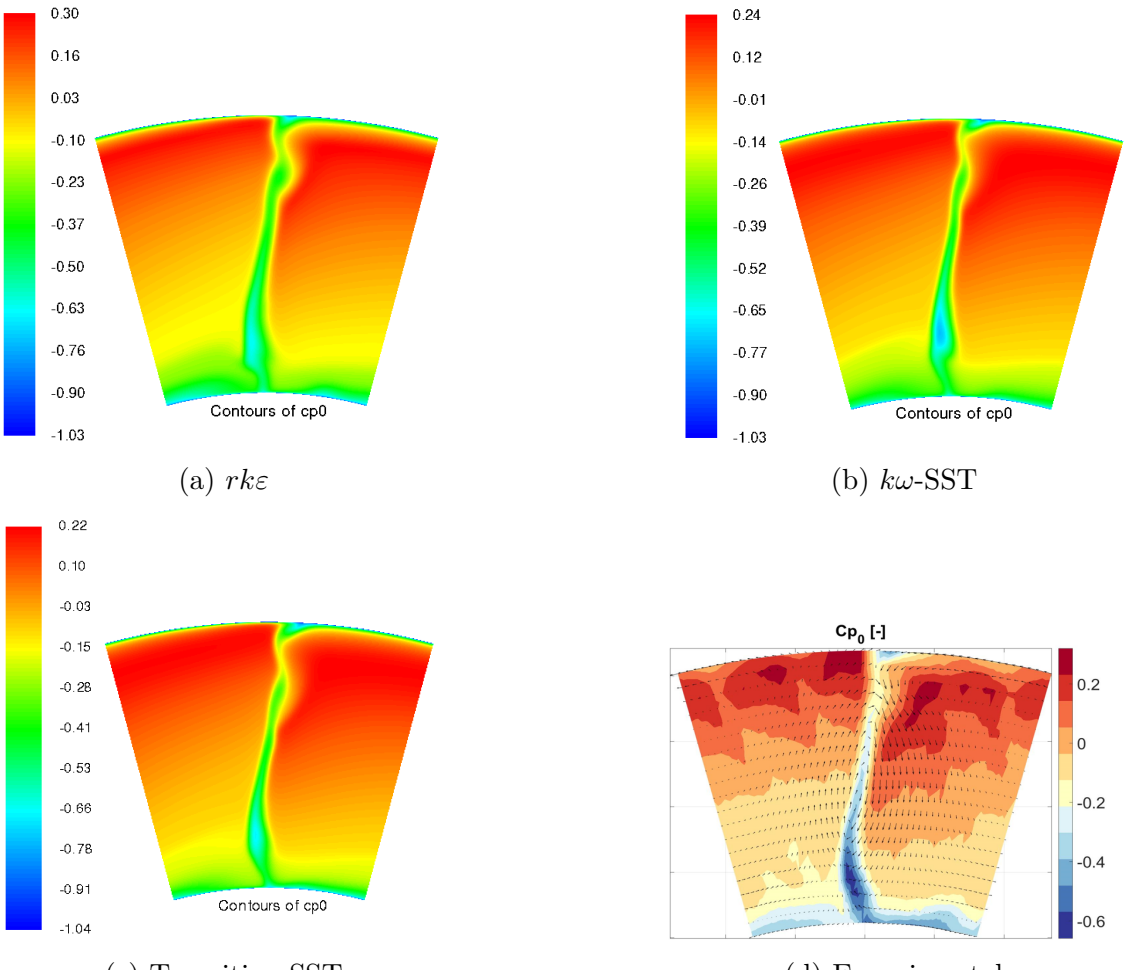

(a) $rk\varepsilon$ (b) $k\omega$-SST

(c) Transition-SST (d) Experimental

Figure A.4: Total pressure coefficient contours at the DS measurement plane for different turbulence models: ADP+5 low Reynolds case

ADP+10

The results of the off-design point ADP+10 are presented below.

Low Reynolds case

Considering the low Reynolds ADP+10 case the blade loading is presented in figure A.5. The $rk\varepsilon$ and $k\omega - SST$ models show a close match at all three spans. It seems like the off-design conditions run for the low Reynolds number has not affected the accuracy of the approximation significantly.

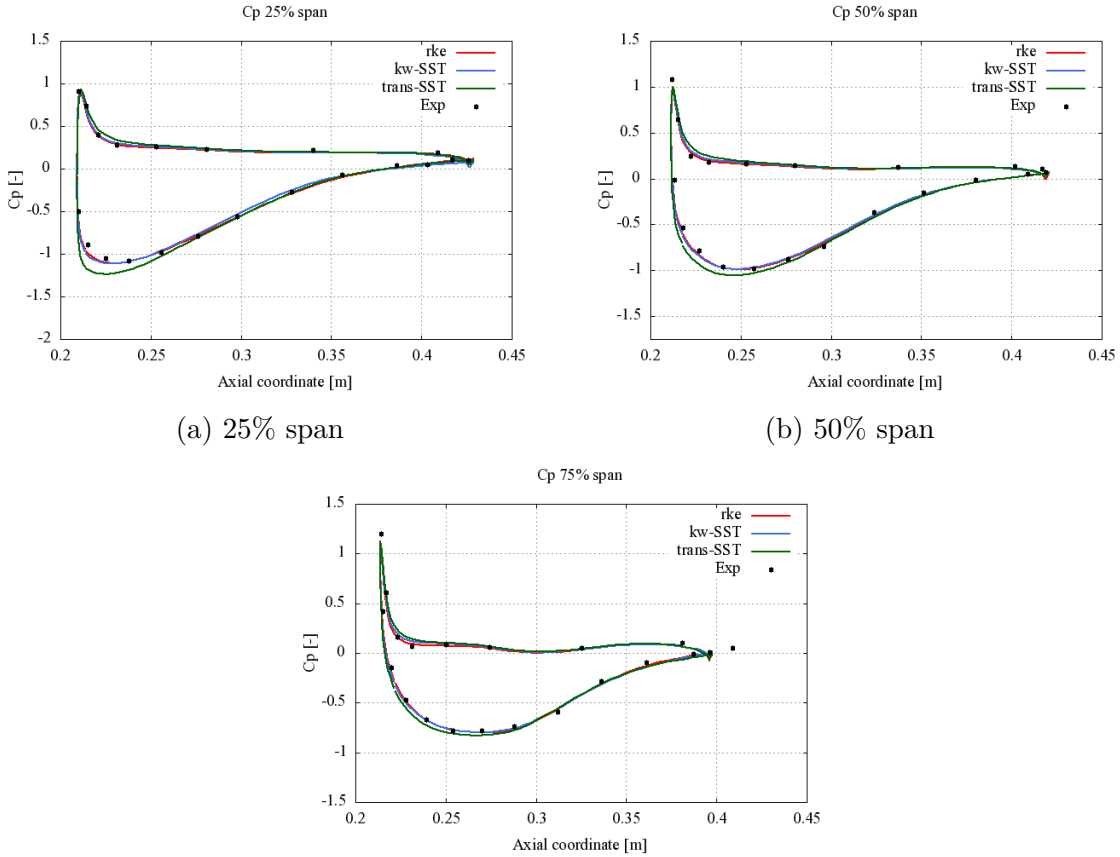

(a) 25% span

(b) 50% span

(c) 75% span

Figure A.5: Blade loading at different spans: ADP+10 low Reynolds case

Figure A.6 shows the radial profiles of swirl at the US and DS measurement planes. The US plane has a good match whereas again the DS plane shows an offset of about 2 degrees.

The radial profiles of total pressure coefficient in figure A.7 shows a close match at

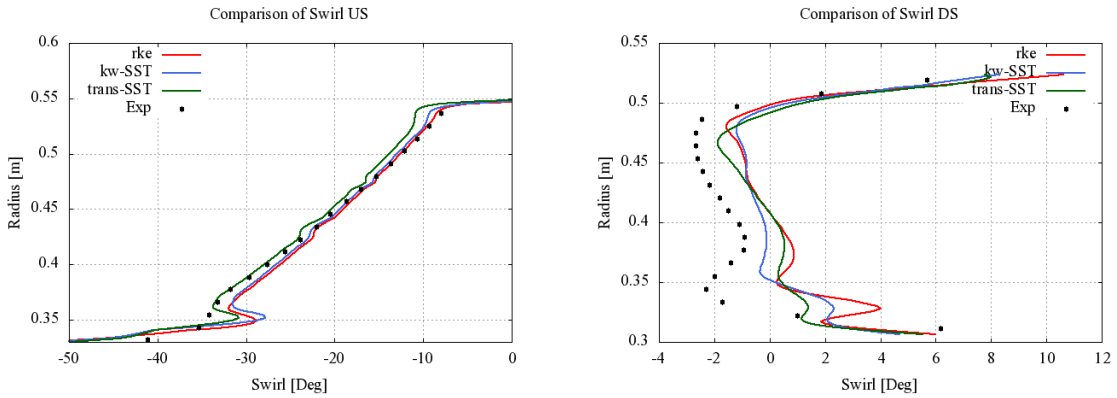

(a) US (b) DS

Figure A.6: Swirl angle at US and DS measurement planes: ADP+10 low Reynolds case

the US measurement plane but a small underestimate below 50% span at the DS measurement plane. This could be due to stronger secondary effects near the hub at off-design conditions. [12]

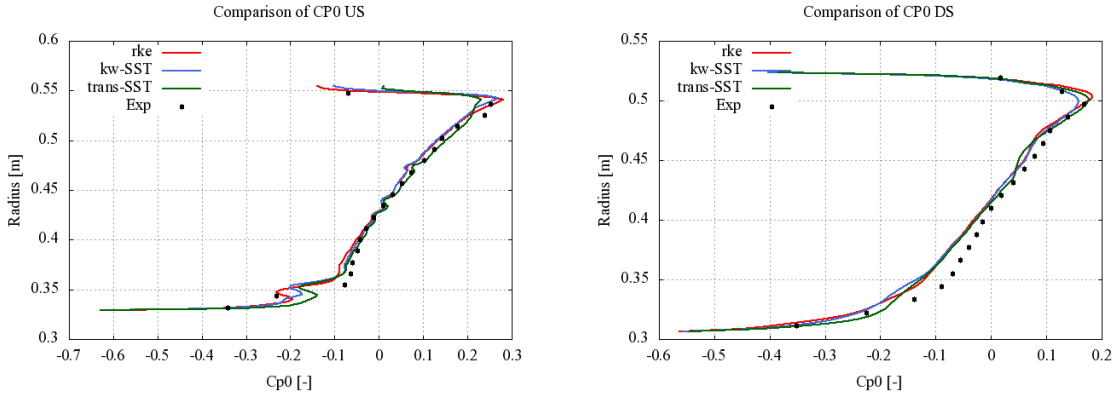

(a) US (b) DS

Figure A.7: Total pressure coefficient at US and DS measurement planes: ADP+10 low Reynolds case

The total pressure coefficient contours in figure A.8 show the shape of the wake fairly well matched in the transition-SST model while the size of the wake at about 25% span is most closely matched by the $k\omega - SST$ model.

High Reynolds case

The blade loading of the high Reynolds ADP+10 case in very well matched after about 15% axial span, as can be seen in figure A.9. Some of the data points are

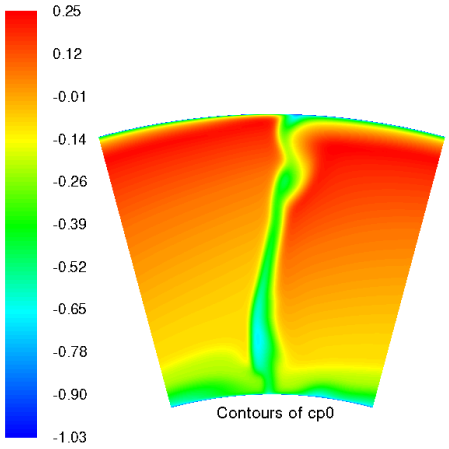

(a) $rk\varepsilon$

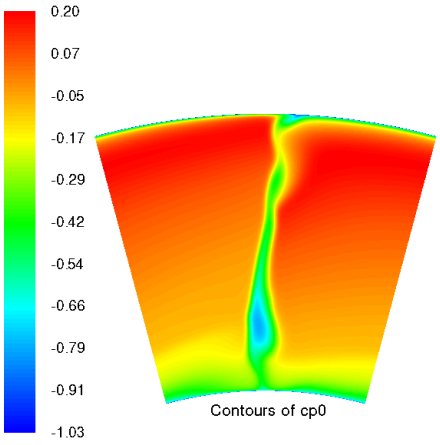

(b) $k\omega$-SST

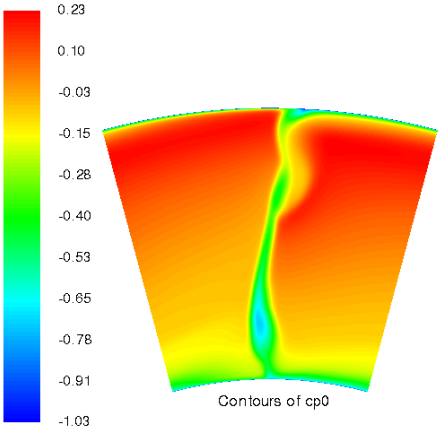

(c) Transition-SST

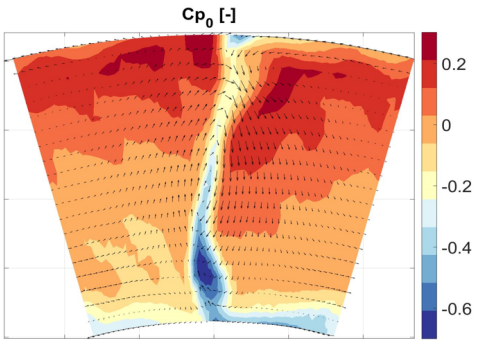

(d) Experimental

Figure A.8: Total pressure coefficient contours at the DS measurement plane for different turbulence models: ADP+10 loew Reynlods case

deviated from close to the leading edge. This is especially seen in the 75% radial span case.

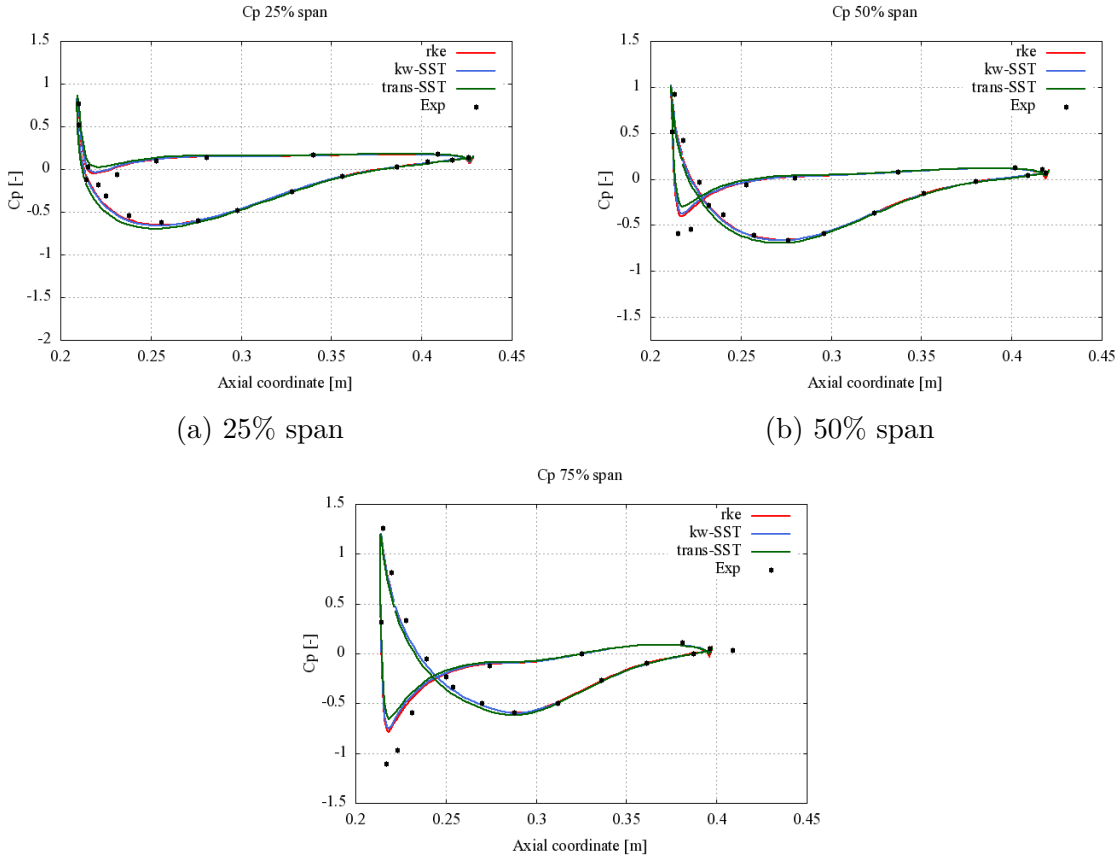

(a) 25% span

(b) 50% span

(c) 75% span

Figure A.9: Blade loading at different spans: ADP+10 high Reynolds case

Here the US measurement plane radial swirl profile is offset by about two degrees while the DS measurement plane radial swirl profile i better matched. The radial profiles of swirl at the two planes are shown in figre A.10.

The radial profiles of total pressure coefficient are shown in figure A.11. The approximations are close both at the US plane and DS plane. The $k\omega$ case is seen to give the closest approximation to the total pressure coefficient at the US measurement plane for this case.

For the total pressure coefficient contours shown in figure A.12 the $rk\varepsilon$ and transition-SST models give a good match of the wake shape. However, for all three turbulence models the large part of the wake near about 15% span is missed.

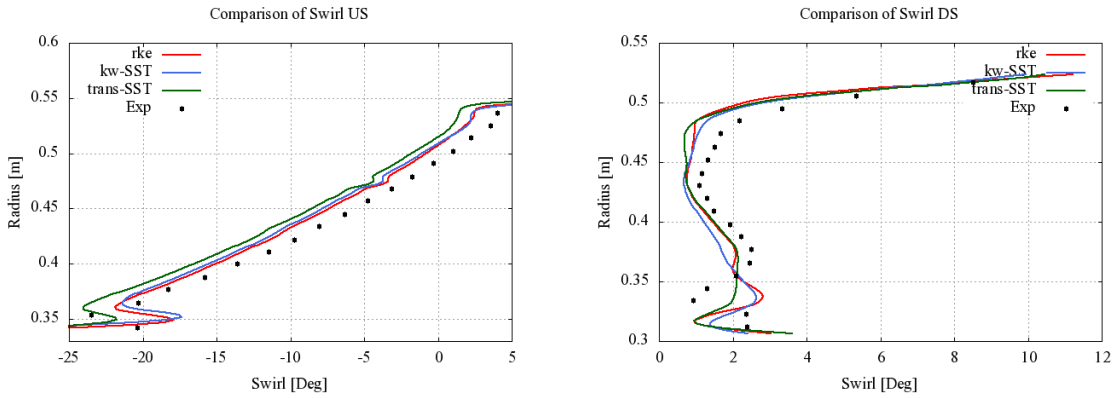

(a) US (b) DS

Figure A.10: Swirl angle at US and DS measurement planes: ADP+10 high Reynolds case

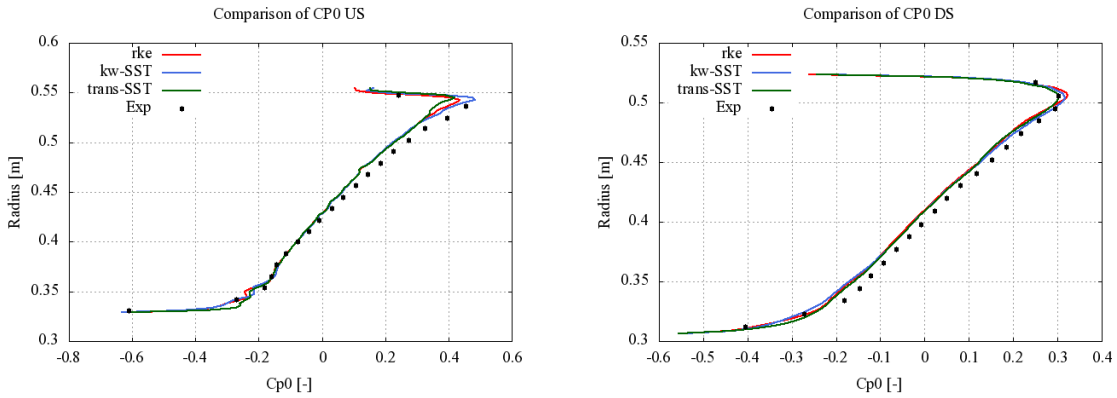

(a) US (b) DS

Figure A.11: Total pressure coefficient at US and DS measurement planes: ADP+10 high Reynolds case

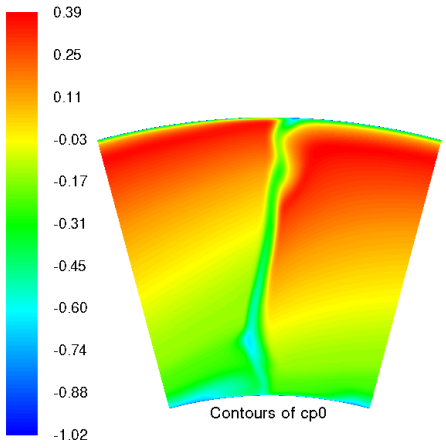

(a) $rk\varepsilon$

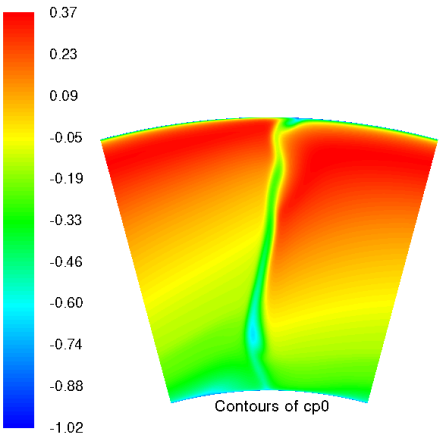

(b) $k\omega$-SST

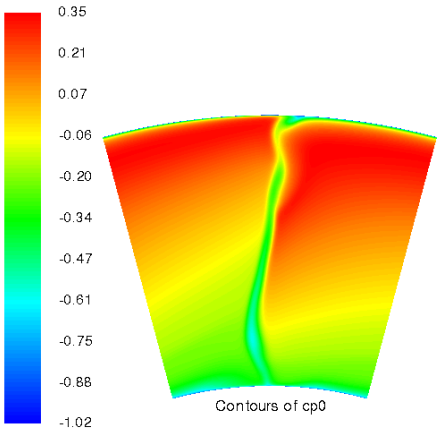

(c) Transition-SST

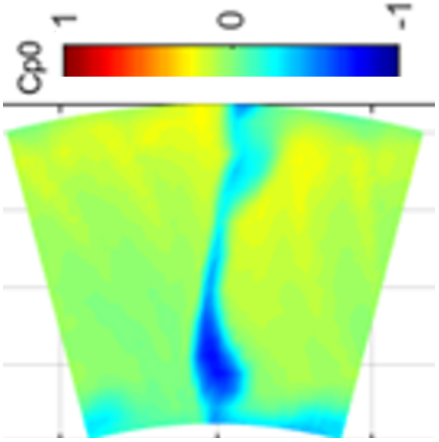

(d) Experimental

Figure A.12: Total pressure coefficient contours at the DS measurement plane for different turbulence models: ADP+10 high Reynolds case

ADP-10

Finally, the results of the off-design point ADP-10 is presented in this section.

High Reynolds case

For the final case, ADP-10 with high Reynolds number, the blade loading is shown at the same spans as before in figure A.13. In this case the difference between the turbulence models is quite pronounced with the $rk\varepsilon$ model giving the closest match to the test data.

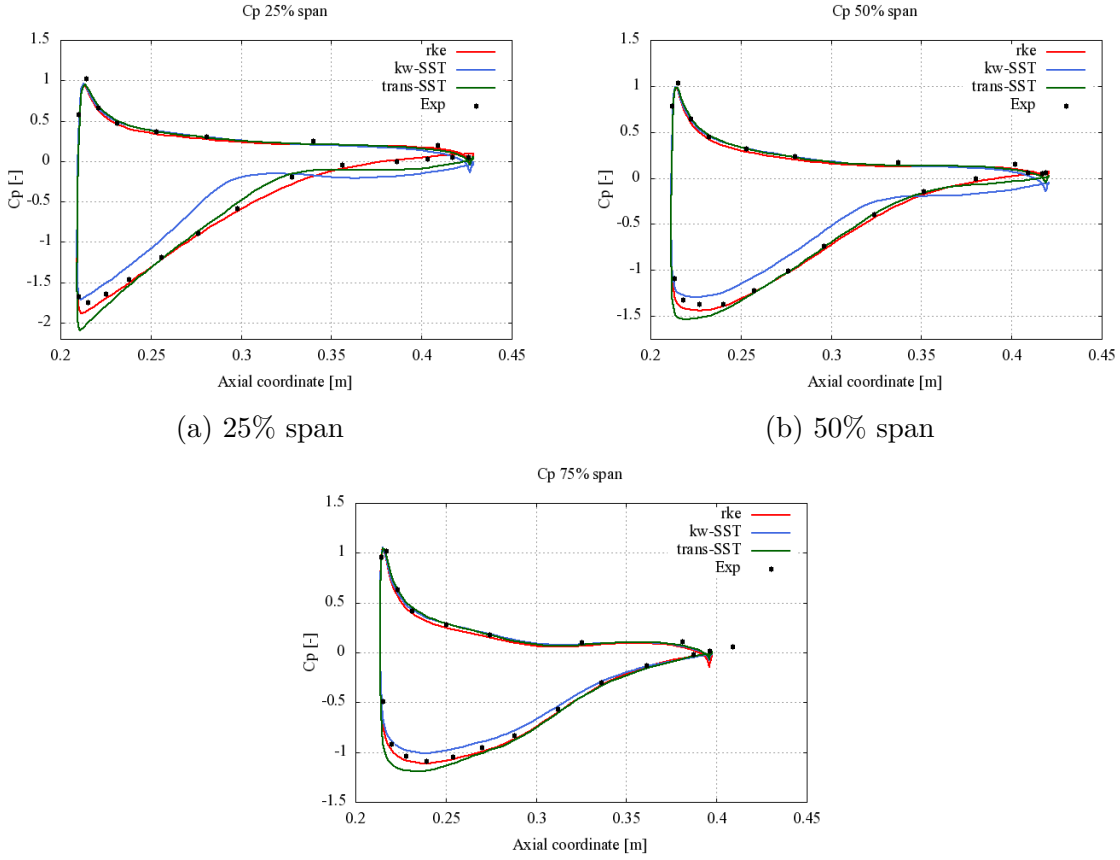

(a) 25% span

(b) 50% span

(c) 75% span

Figure A.13: Blade loading at different spans: ADP-10 high Reynolds case

Figure A.14 shows that the swirl at both the US measurement plane and DS measurement plane is well matched. The $rk\varepsilon$ model gives the closest match at the US measurement plane while the transition-SST model gives the overall best match at the DS measurement plane.

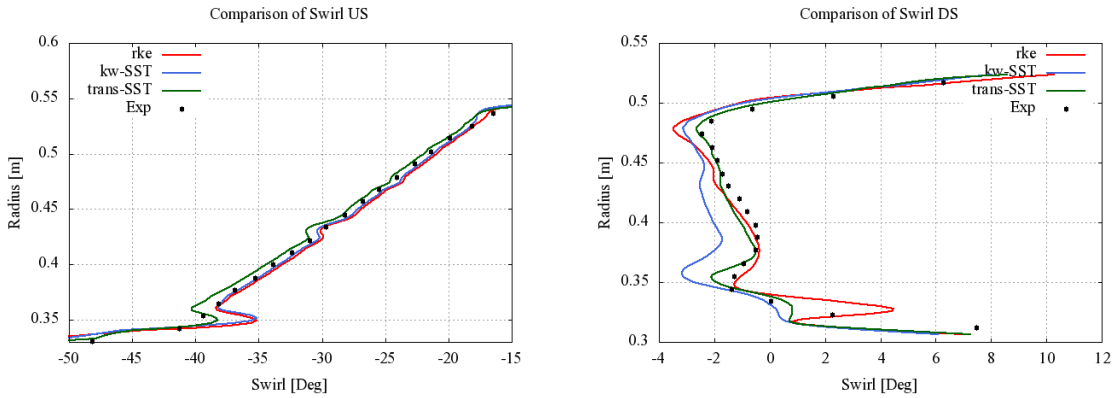

(a) US (b) DS

Figure A.14: Swirl angle at US and DS measurement planes: ADP-10 high Reynolds case

For the radial profiles of total pressure coefficient in figure A.15 all three turbulence models underestimate the total pressure coefficient att both measurement planes.

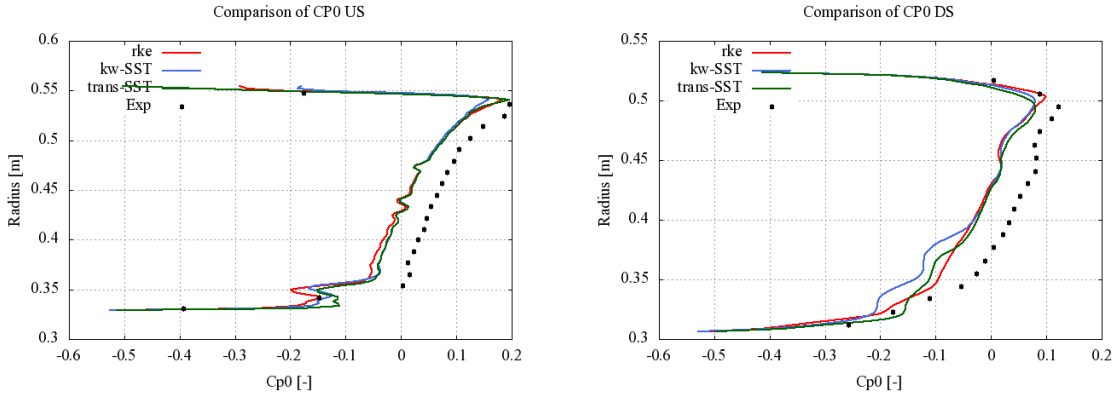

(a) US (b) DS

Figure A.15: Total pressure coefficient at US and DS measurement planes: ADP-10 high Reynolds case

Finally, the total pressure coefficient contours at the DS measurement plane in figure A.16 show the $k\omega$ model greatly overestimating the size of the low pressure region near 15% span whereas the transition model capture the size and shape of the wake fairly well.

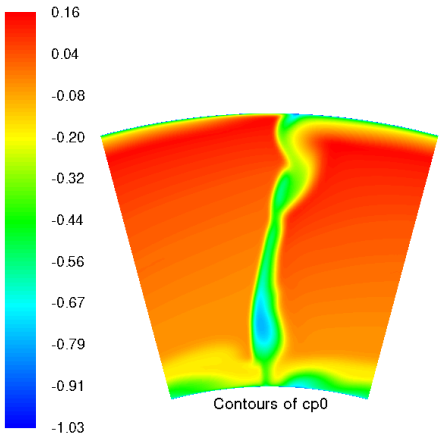

(a) $rk\varepsilon$

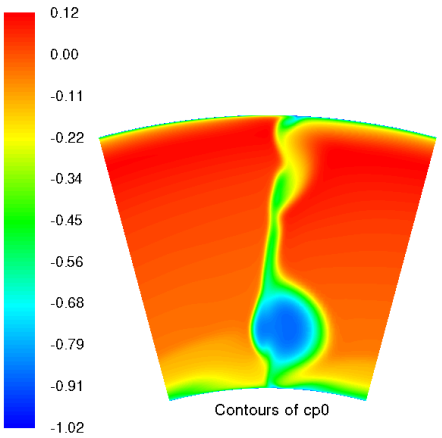

(b) $k\omega$-SST

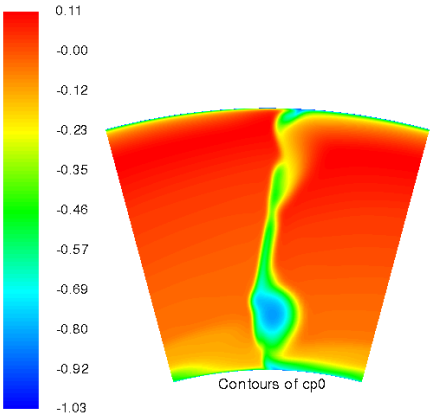

(c) Transition-SST

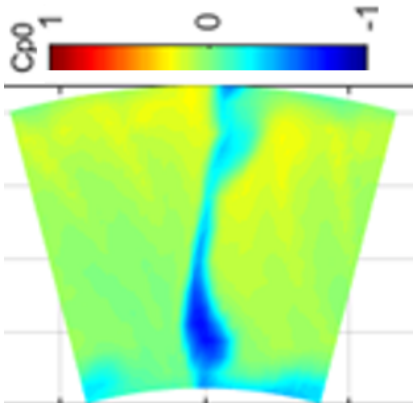

(d) Experimental

Figure A.16: Total pressure coefficient contours at the DS measurement plane for different turbulence models: ADP-10 high Reynolds case